12-2004

Investigation of Zircaloy-4 Doped with Metallic Burnable Poisons

Chrysostomes K. Kahambwe
University of Tennessee, Knoxville

To the Graduate Council:

I am submitting herewith a thesis written by Chrysostomes K. Kahambwe entitled "Investigation of Zircaloy-4 Doped with Metallic Burnable Poisons." I have examined the final electronic copy of this thesis for form and content and recommend that it be accepted in partial fulfillment of the requirements for the degree of Master of Science, with a major in Nuclear Engineering.

Martin L. Grossbeck, Major Professor

We have read this thesis and recommend its acceptance:

Laurence F. Miller, Lawrence W. Townsend

Accepted for the Council:
Carolyn R. Hodges

Vice Provost and Dean of the Graduate School

(Original signatures are on file with official student records.)

To the Graduation Council:

I am submitting herewith a thesis written by Chrysostomes K. Kahambwe entitled "Investigation of Zircaloy-4 Doped with Metallic Burnable Poisons". I have examined the final paper copy of this thesis for form and content and recommend that it be accepted in partial fulfillment of the requirement for the degree of Master of science, with a major in Nuclear Engineering.

Martin L. Grossbeck, Major Professor

We have read this thesis
and recommend its acceptance

Laurence F. Miller

Lawrence W. Townsend

Accepted for Council:

Vice Chancellor and
Dean of Graduate Studies

INVESTIGATION OF ZIRCALOY-4 DOPED WITH METALLIC BURNABLE POISONS

A Thesis

Presented for the

Master of Science

Degree

The University of Tennessee, Knoxville

Chrysostomes K. Kahambwe

December 2004

DEDICATION

I want to thank God for the opportunity he gave me in working this thesis. I went through ups and downs during the course of my life, but God has never abandoned me. So, this thesis is dedicated to Eliane Kahambwe, my wife

"This explains why a man leaves his father and mother and is joined to his wife, and the two are united into one. Since they are no longer two but one, let no one separate them, for God has joined them together."

Reference: Matthew 19:5-6

ACKNOWLEDGEMENT

This thesis could not have been completed without the help and support of my advisor, Dr. M. L. Grossbeck. I would like to express my deepest gratitude to him for the many hours he spent with me on this project.

Also, a great thanks to the other members of my committee, Dr. L. Miller, and Dr. L.W. Townsend for their suggestion and accepting serving in my committee, and Dr. H. L. Dodds for accepting me in the Nuclear Engineering Program. I thank him for all of his support.

Appreciation is also expressed to many personnel of the Scanning Electron Microscopy, Material Engineering Laboratories, and Nuclear Engineering Machine Shop, at Engineering and Science Building and U.T.N.E. Department. Specifically, G. Jones, M. Robert, F. Douglas, R. Bailey and G. Graves.

In addition, I wish to express my appreciation to the Department of Energy for providing financial support for this project via a research contract with the University of Tennessee Knoxville, Department of Nuclear Engineering and the National Academy for Nuclear Training.

Finally, I must thank my parents, C. P. Kasongo and A. K. Safalani and my children, K. S. Kahambwe, K.T. Kahambwe and K. K. Kahambwe for all of their support.

ABSTRACT

Burnable poisons are used in all commercial reactors to level the power distribution and to reduce the requirements for an excessively large control system. It has been proposed that metallic rare earth elements, serving as burnable poisons, might be alloyed with the fuel cladding rather than mixed with fuel in the form of compounds. This research project studies the effect of such additions on the ductility and the corrosion resistance of three such alloys.

Alloys of Zircaloy-4 with 0.5 % Gd, 2.0 % Dy, and 2.0 % Er, chosen to represent the maximum likely concentrations of the absorbing elements to be used in a nuclear reactor, were melted and rolled into sheet. Tensile tests were conducted to obtain a quantitative measure of ductility. In addition, coupons were exposed to superheated steam in an autoclave to test the corrosion resistance of the alloys. Only the Gd alloy survived the test. Scanning electron microscopy and energy dispersive x-ray analysis were conducted to investigate the possibility of second phase formation and segregation of the rare earth elements in an attempt to elucidate the mechanism of failure of the alloys.

TABLE OF CONTENTS

LIST OF TABLES

LIST OF FIGURES

FIGURE **PAGE**

FIGURE **PAGE**

FIGURE **PAGE**

Chapter 1

INTRODUCTION

1.1. Background

Burnable poisons are used in all commercial reactors to aid in reactivity control, to reduce local power peaking, and optimize fuel utilization. At the beginning of the cycle, a reactor core is loaded with fresh fuel, which must contain excess reactivity to compensate for fuel depletion, fission product poisons, and temperature effects that create negative reactivity [1]. Current technology uses control rods and burnable poisons to control excess reactivity in the core. Fixed burnable poisons are generally used in the form of chemical compounds of boron, gadolinium, and other rare earths that are shaped into separate lattice pins or plates. These materials can be considered as additives and are usually distributed more uniformly than control rods and become less disruptive to the core power distribution. It has been proposed that metallic rare earth elements, serving as burnable poisons, might be alloyed with the fuel cladding rather than mixed with fuel in the form of compounds [2]. Alloying Zircaloy-4 with metallic rare earth elements and studying the effect of such additions on ductility and corrosion behavior are required. In this study, samples were exposed to high temperature steam, and Scanning Electron Microscopy (SEM) and Energy Dispersive x-ray (EDX) analysis were performed to determine the mode failure of the alloys.

1.2 Reactivity Control

Control materials are used in a nuclear reactor to absorb neutrons in order to control the reactivity in a desirable manner. There exist three common ways in which control materials may be used. First, movable rods are used to adjust and maintain the reactivity at a desired value at any time during the operation of the reactor. Second, burnable poisons are built into the core in fixed positions. Third, chemical shims, also known as soluble poisons, which produce uniform neutron absorption, are dissolved in the water coolant. Boric acid, known as boron soluble, is considered to be the most common soluble poison in commercial pressurized water reactors. When present in the coolant, the thermal utilization factor decreases, causing a decrease in reactivity. By changing the concentration of boric acid in the coolant, the reactivity of the core can be varied. When the boron concentration is increased, the coolant absorbs more neutrons, adding negative reactivity. On the other hand, the positive reactivity is increased when the boron concentration is reduced. The variation of boron concentration in a PWR is a slow process that is used to counterbalance fuel burnout. In normal operation of a PWR, expansion of the coolant, which also serves as a moderator, causes insertion of negative reactivity. If a high concentration of boron were dissolved in the coolant, expansion of the coolant would lead to less boron in the reactor, thus introducing positive reactivity. Therefore, there is a limitation on the concentration of boron that can be tolerated in the reactor coolant. As a result, a chemical shim alone cannot take the place of a burnable poison.

Control rods cannot be used alone to compensate for the excess reactivity for several reasons. First, they take up room that would otherwise be used for fuel. Second, they lead to the requirement of inserting regulating control rods deep into the core to offset the excess fuel, thus producing non-uniform power distribution throughout the core life where most of the power is produced in a small fraction of the core volume early in life. To control large amounts of excess fuel without adding additional control rods, burnable poisons are incorporated throughout the core to remove neutrons by absorption. This leads to a more uniform power distribution. The ideal burnable poison would be one that has properties corresponding to the fuel depletion characteristics. This requirement is achieved when the poison's absorption cross section is greater than the fuel cross-section during the first part of the fuel cycle, and the poison is completely burned during the last part of the cycle. An alternative is using lumped or heterogeneous poisons to make the reactivity of a poison material more uniform over core life through the use of self-shielding. In this process, the poison is considered to be thick enough that only the external layer of the poison is exposed to the neutron flux. Absorption in the external layers reduces the number of neutrons entering the internal material. When the external layers of poison absorb neutrons and are converted to non-poison materials, the internal layers start absorbing more neutrons, and the negative reactivity of the poison material is fairly uniform [2].

The most widely used burnable poisons in all commercial nuclear reactors are elements such as gadolinium, erbium and boron. These materials suffer from two common disadvantages. First, the rare earths result a small residual negative reactivity

which leads to earlier refueling. Secondly, boron transmutes to helium, which is insoluble and creates undesirable internal fuel pin pressure. The transmutation absorption reaction is described as follows.

$$^{10}B + ^{1}n \rightarrow ^{7}Li + ^{4}He \quad (1.1)$$

A sufficiently high burnup, the combination of fission product gases and helium from boron transmutation will produce a pressure higher than the reactor coolant pressure. If this happens, the cladding will creep away from the fuel resulting in an undesirable increase in the centerline temperature. This problem can be partially solved by simply spreading the boron BP's over all fuel rods, reducing the amount of boron in each of the fuel rods that contain the poison. This process increases cost and increases the burnup rate of the boron burnable absorber. One way to resolve the helium issue is to use other burnable absorbers.

Gadolinium is one of the rare earth elements which possess a high neutron absorption cross section and a burnup rate that can be made to correspond to that of the ^{235}U isotope used as nuclear fuel [3]. From isotopic perspective, ^{157}Gd (15.8 % natural isotopic abundance) with 61,000 barns (Average over a PWR Spectrum) thermal cross section transmutes to ^{158}Gd, which has a thermal absorption cross section of only a few barns. As gadolinia (Gd_2O_3) doped UO_2 neutron absorber material has been successfully proven to extend the lifetime of a reactor core and level the power distribution in commercial reactors, it has been selected as one element for the present study.

Dysprosium is another candidate burnable poison which is composed of several stable isotopes. ^{164}Dy (28.1% natural abundance and 2,650 barns thermal cross section) exhibits better characteristics than the majority of stable dysprosium isotopes. The use of dysprosium fully enriched in ^{164}Dy will enhance the quality of dysprosium based burnable poisons in pressurized water reactors. As ^{164}Dy possesses a much larger thermal cross section than the other stable isotopes, dysprosium enriched in ^{164}Dy leads to a reduction of the residual reactivity at the end of fuel life [4]. Finally, ^{164}Dy has an uniform burnup rate over a period of 4 years which makes it a candidate for use in generation IV reactors with an extended fuel cycle [2]. Detailed information of the other stable isotopes is provided in Table 1.1

Table 1.1: Stable dysprosium isotopes

Isotope	Natural Abundance (%)	Thermal Cross Section (Thermal Spectrum Average)
^{156}Dy	0.06	33
^{158}Dy	0.1	43
^{160}Dy	2.3	56
^{161}Dy	18.9	600
^{162}Dy	25.5	194
^{163}Dy	24.9	124

Erbium also has isotopes with high absorption cross sections, ^{167}Er (22.9% natural isotopic abundance) shows a large neutron cross section with 660 barns thermal cross section that produces ^{168}Er with a very small thermal cross section. Besides ^{167}Er and ^{168}Er, erbium has several isotopes that have smaller capture cross sections, which are difficult to burn out and thus have a residual negative reactivity at the end of reactor core life. Erbium is currently used in the form of oxide powder which is homogeneously mixed into UO_2 , enabling a pressurized water reactor to operate with a 2 year reload cycle [5]. Table 1.2 presents a summary of the natural isotopic abundance and thermal cross section of other erbium isotopes.

Table 1.2: Stable erbium isotopes

Isotope	Natural Isotopic Abundance (%)	Thermal Cross Section (Thermal Spectrum Average)
^{162}Er	0.14	19
^{164}Er	1.6	13
^{166}Er	33.4	19.6
^{170}Er	14.9	5.8

An ongoing research project is focused on alloying metallic rare earth elements, serving as burnable poisons, with the fuel cladding rather than mixing the BP's with fuel in the form of chemical compounds. A goal of this research is to investigate the effect of such additions on the ductility and the corrosion resistance of three such alloys.

1.3. Review of Current Burnable Poison Configurations

Several types of burnable poison designs have been used in PWR's. One method used by both Westinghouse and Framatome is to use boron carbide (B_4C) in non-fueled rods. The burnup characteristics of B_4C assemblies depend on concentration of B_4C in a given rod. Experience has shown that B_4C burns more slowly than gadolinium because its absorption cross section is about one decade smaller than that of Gadolina (Gd_2O_3) without isotope enrichment [6]. Westinghouse has produced two major forms of burnable poisons: Pyrex Burnable Absorber Assemblies (BAA) and Wet Annular Burnable Absorber (WABA). The BAA configuration uses borosilicate glass (B_2O_3 – SiO_2 with 12.5 w % of B_2O_3 in the form of Pyrex) clad in 304 stainless steel. The WABA configuration utilizes annular pellets of B_4C-Al_2O_2 that contain 14w % of B_4C clad in Zircaloy [6]. Framatome Cogema Fuels uses Burnable Poison rods made of B_4C-Al_2O_3 pellets contained in Zircaloy tubing. When comparing the WABA to the BAA configuration, Wagner and Parks [7] reported that the BAA burnable poison rods displace a greater volume of water and result in a larger effect on reactivity. An illustration of a segment of a Westinghouse 17X17 assembly lattice with WABA used for modeling by the HELIOS code is shown in Figure 1.1[7]. Another type of burnable poison used in PWR's is the Integral Burnable Absorber in which neutron absorbers such as gadolinia

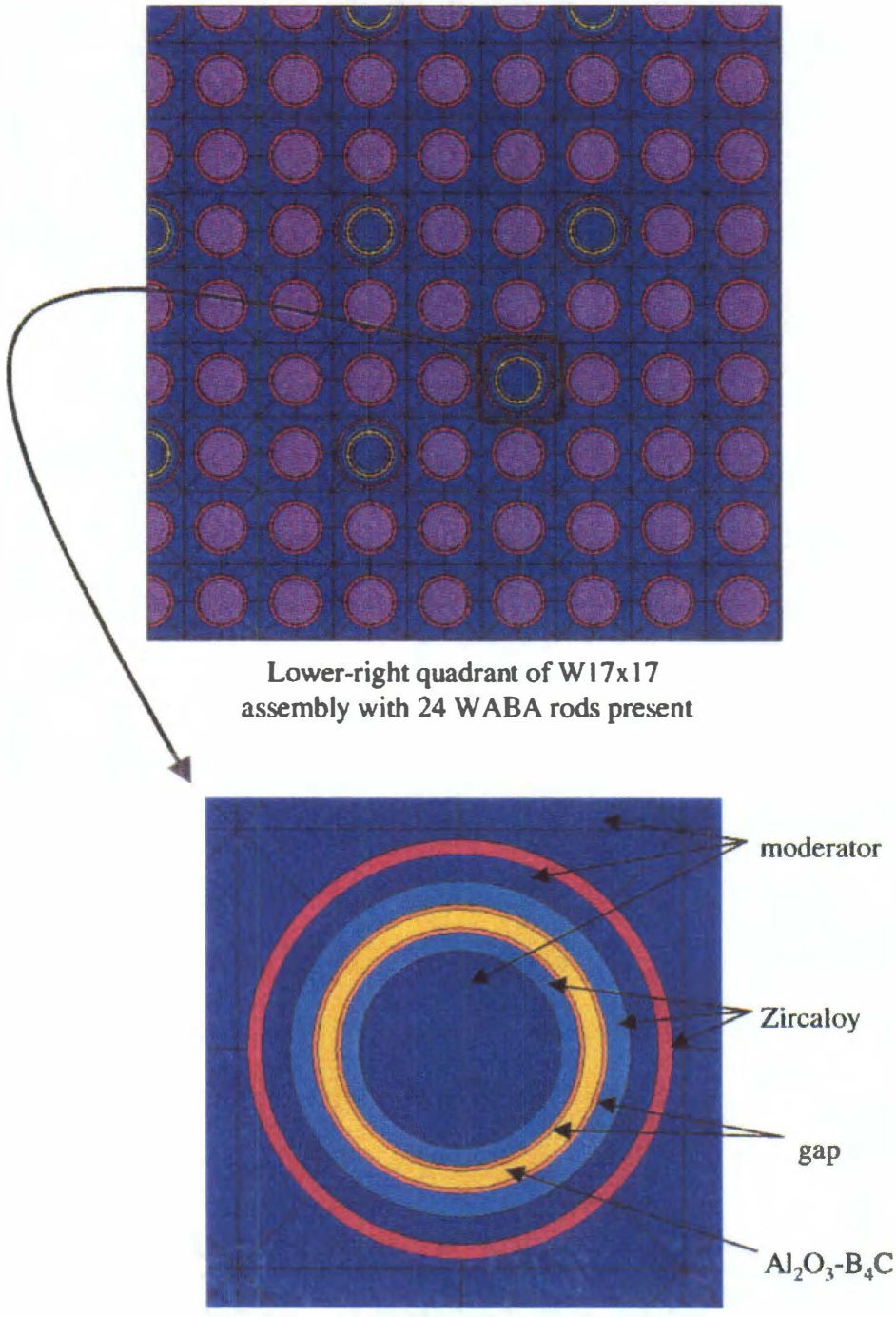

Figure 1.1: Illustration of a segment of lattice assembly with WABA BPRs used to model with the HELIOS code, J. C. Wagner and C.V. Parks, Parameter Study of Effect of the Burnable Poison Rods for PWR Burnup Credit

(Gd_2O_3) or erbia (Er_2O_3) are mixed directly with the uranium dioxide (UO_2) fuel in a specific rod within an assembly. Gadolinia (Gd_2O_3) burnable poison is incorporated also in BWR's homogeneously mixed in the fuel pellets of a number of fuel rods [6]. O'Leary and Pitts reported that fuel designs using gadolinia may incorporate approximately 20 Gd_2O_3 -UO_2 fuel rods in a single fuel assembly while fuel designs using erbia may require as many as 90 Er_2O_3 - UO_2 fuel rods in a single fuel assembly [6]. zirconium diboride (ZrB_2) is another non-removable burnable poison used in PWR's by Westinghouse.

With the end of Cold War, reduction in nuclear arsenals was necessary to decrease a surplus of nearly 100 tons of weapons grade plutonium. This led to a proposal of using surplus plutonium as fuel for nuclear reactors. The Canadian Deuterium (CANDU) reactors have been an optimal choice for burning weapons grade plutonium as mixed oxide (MOX) due to their capability for continuous refueling. Scientists stated that to burn safely in CANDU the plutonium must be transformed into oxide and alloyed with dysprosium burnable poison. The transformation of plutonium into oxide increases the amount of plutonium needed to obtain a particular burn rate, decreases the local peak power and the local positive moderator void coefficient (MVC) have in the middle of the fuel bundle. Thus, dysprosium changes the bundle configuration and makes the MVC more negative [2].

1.4. Research Objectives

This research provides experimental studies for evaluating the effect of alloying fuel cladding material, Zircaloy-4, with metallic rare earth elements, such as dysprosium, erbium and gadolinium. It investigates the effects of additions of these rare earth elements on ductility and corrosion resistance. Since corrosion failures cause reduction of life of the fuel cladding including contamination by radioactive materials, it is very important to determine corrosion resistance of fuel cladding [8]. Corrosion resistance was evaluated by autoclave testing with superheated steam, and ductility was evaluated by tensile testing.

1.5. Scope and Organization

This research is presented in seven chapters. The first chapter presents a general background of burnable poisons used in commercial nuclear reactors. Chapter 2 provides a detailed discussion of zirconium alloys as a reactor material and development of the Zircaloy alloys. Chapter 3 presents the fabrication procedures and specimen description. Chapter 4 discusses corrosion testing of the zirconium alloys. Chapter 5 discusses optical microscopy, specimen preparation for light microscopy, optical microstructural analysis, scanning electron microscopy, and sample preparation mechanical properties. Chapter 6 discusses tensile testing and fractography analysis. Chapter 7 contains conclusions and suggestions for future work.

Chapter 2

ZIRCONIUM ALLOYS

2.1. Zircaloy as a Reactor Material

Zirconium alloyed with other metallic elements is a very promising metal for use as a basic structural and fuel-cladding material in thermal reactors, at temperatures up to about 450°C (842°F) limited by corrosion behavior. Several requirements for a material to be used in water-cooled and moderated nuclear reactors are low neutron absorption, creep resistance, corrosion resistance, fabricability, and compatibility with fuels. Zirconium possesses a high melting point, sufficient strength, good thermal conductivity, low thermal expansion, low cross section for capture of thermal neutrons and excellent corrosion resistance [9]. As a consequence, it is used in commercial nuclear reactors primarily for its low neutron absorption cross section and excellent high temperature properties. Zirconium is in group IVA of periodic table and experiences an allotropic transformation from hexagonal close packed (hcp) to a body cubic center (bcc) phase when heated above 862°C (1583.6°F) [10]. Its most important application is for fuel cladding. Generally, zirconium extracted from the ore contains approximately 0.5 to 3.0 percent of hafnium which has a high thermal neutron cross section (Thermal Spectrum Average). It is important that most of the hafnium be removed from zirconium for use in the thermal reactors [11]. Nuclear power generation applications use for more than 90% of the commercial zirconium production, with reactor grade zirconium being essentially hafnium free. Zirconium is also used in the chemical industry, but in this application it is

not necessary to remove hafnium as is done to produce nuclear grade Zirconium. Zirconium is usually manufactured by the Sponge or Kroll process in which the metal is made by the reduction with magnesium [11].

One of the outstanding properties of zirconium that will be considered in this investigation is the metal's ability to resist corrosion in high temperature water and steam. It also resists attack by most acids, alkalis and salts in aqueous solution under all reasonable conditions. Corrosion resistance of zirconium in water at high temperatures is important from the reactor standpoint. However, it should be pointed out that the corrosion behavior of zirconium alloys is very sensitive to the presence of impurities and markedly dependent on the composition of the alloy [12].

There are several fabrication techniques, such as machining, hot and cold rolling, forging, extrusion, and drawing that can be utilized with zirconium when reasonable means are taken to prevent oxidation. As hot operations have the advantage of easy size reduction, zirconium ingots are hot rolled as the initial operation. The metal can also be cold-worked, followed by annealing in vacuum or in an inert atmosphere to avoid contamination by oxygen and nitrogen from air. Powder-metallurgical methods can also be performed to make zirconium parts. Such parts fabricated from powder have highly satisfactory mechanical properties [12]. In addition, zirconium metal has excellent welding characteristics but the operation must always be conducted in an atmosphere of high purity inert gas.

Fission of the fissile materials in the fuel results in the production of radioactive fission products, of which solid fission products are retained in the fuel matrix and gaseous fission products may diffuse from the fuel and be released into the coolant system. This represents a major concern to the public. It is important to prevent the release of these fission products from the fuel. This can be accomplished by sealing the fuel "pins" of a cladding material such as Zircaloy. Besides having high thermal conductivity, low neutron absorption cross section, good multi axial rupture strength, and zirconium also has the advantages of having high thermal conductivity, good creep strength and high ductility. Furthermore, a common failure mode for fuel rods is pellet-cladding interaction (PCI) which results from interaction between the fuel and cladding in a corrosive environment. Vapors of cesium and iodine are released to the gap and may corrode the interface and result in Stress Corrosion Cracking (SCC) of the inner surface of the cladding [13].

A new fuel design incorporates a pure zirconium liner on the inside surface of the clad. Pure zirconium is more easily worked than Zircaloy and can adapt to the sharp features of the fuel to minimize early failure [14]. A process known as hydriding of Zircaloy cladding may also cause fuel failure. Zircaloy alloy has an extremely high affinity for hydrogen. When it reacts with water, a thin film of zirconium oxide (Zr_2O) is formed on the external surface by interaction of the clad with the coolant. The rate of this reaction is largely dependent on partial pressure of hydrogen and can only happen in areas of low oxygen concentration in the coolant [13].

2.2. Development of the Zircaloys

2.2.1. Introduction

Although several metallic elements were tested for use as structural materials in the cores of water- cooled reactors, only aluminum and magnesium met the low cross section requirement [12]. However, at high temperatures, both materials fail to meet the requirements of strength and corrosion resistance. Since zirconium's mechanical properties had proven to be adequate for nuclear application, these facts, combined with its low cross section to thermal reactors, led to the selection of zirconium as the material to be used in water- cooled and moderated nuclear reactors [8]. Since it was a concern that radiation fields in a reactor would accelerate the corrosion process, a study was performed to analyze the corrosion resistance of zirconium, which led to a family of zirconium-base alloys known as Zircaloys. The Naval Reactors Branch and the Pittsburgh Naval Reactors Office of the US Atomic Energy Commission were two major organizations to develop Zircaloys from high purity metal produced by the Van Arkel process that led to the discovery of Zircaloys -1, -2, and -3 [15]. Crystal bar zirconium produced by the Van Arkel, process is a very high purity and ductile form of zirconium metal that is utilized mostly in research and special applications. The Van Arkel process has been obtained by an iodide decomposition process [11]. It produces the highest purity metal currently available and is most commonly used. Schemel reported that Kaufman and Utermeyer discovered that measurements of the thermal neutron cross section of zirconium exhibited poor performance when the metal tested had not been separated from the hafnium [11]. When hafnium was fully separated, zirconium showed

a very low thermal neutron absorption cross section. This led the US Naval Nuclear Propulsion Program to use hafnium as a control rod material in naval reactors due to its high thermal neutron cross section [11, 15]. Even though hafnium is used in naval reactors, controlled amounts of iron and oxygen are still needed to make sure that strength levels are achieved. Figure 2.1 shows zirconium sponge and crystal bar.

Unalloyed zirconium is weak and contains minor amounts of impurities. Alloying additions were necessary to improve mechanical properties of the material. A certain amount of tin was added in order to suppress the deleterious effects of nitrogen that affected the acceleration of corrosion of crystal bar zirconium.

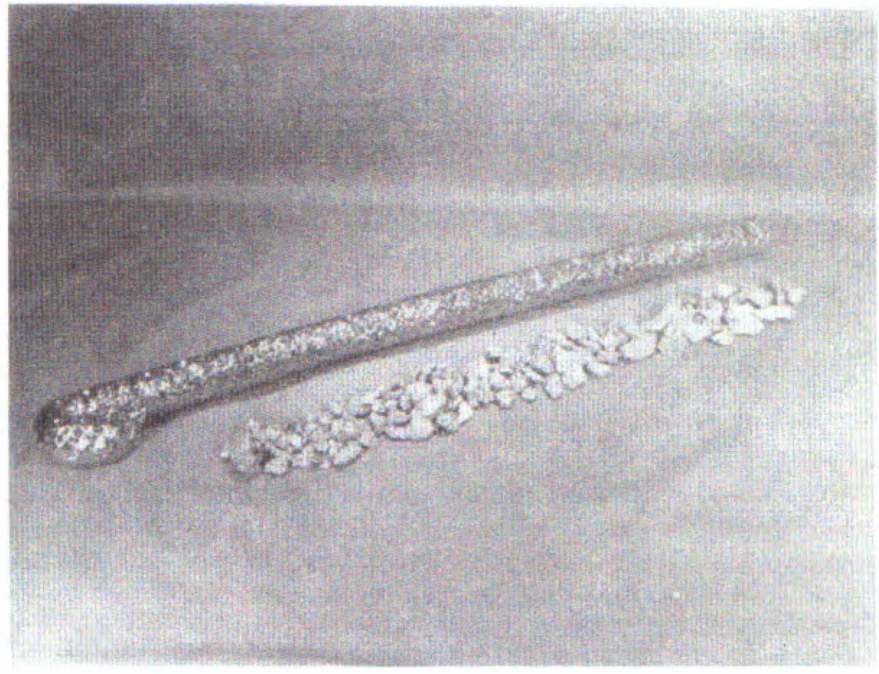

Figure 2.1: Zirconium sponge and crystal bar, J. H. Schemel, ASTM Manual on Zirconium and Hafnium, pp. 6, 1977

The amount of tin needed to lend the most favorable corrosion resistance to zirconium containing interstitial impurities such as nitrogen was dependent on the nitrogen content of the alloy. As zirconium - tin alloys and unalloyed zirconium exhibit the same behavior, it was proposed that another alloy that contained 2.5% tin be developed. The unalloyed zirconium mixed with zirconium – tin that contained 2.5% tin to form Zircaloy-1 [15].

The literature data illustrate that additions of tin to impure zirconium did not produce satisfactory corrosion resistance unless nickel, iron, and chromium were also added to zirconium-tin alloys. The tin content was dropped from 2.5% to 1.5% in order to improve the alloy. Although, a value of 0.22 % of iron was used in binary alloy development, the total alloy content was to be maintained at a minimum in order to facilitate the fabrication, and a value of 0.12% tin was then adopted for the binary alloy. The chromium content was about 0.1% in the binary alloy and indicated that corrosion increased as chromium content increased. The concentration of chromium was fixed at 0.1% to prevent the hardness of the alloy from increasing. Regarding the nickel concentration, a value of 0.25% was used for binary zirconium-nickel alloys. Since nickel increases the corrosion resistance and shows major influence in extending the life of zirconium alloy, 1.5% tin with 0.12% iron and 0.1% chromium were mixed to develop Zircaloy-2 [15].

The fundamental characteristic of Zircaloy-2 is its excellent corrosion resistance in high-temperature water in which it was differentiated from unalloyed zirconium. The corrosion is distinguished by the formation of an adherent zirconium dioxide film that

protects the alloy from further corrosion. This dioxide film can grow at a very low temperature up 482°C (900°F) without changing its structure [11]. The water corrosion of Zircaloy-2 is partially affected by metallurgical treatment, but the resistance to steam at temperatures up 398.8°C (750°F) and above can be disturbed by heat treatment up to 787.7°C (1450°F) or by slow cooling through the two-phase region, 787.7°C to 1015.5°C (1450 to 1860°F) [15]. A few years later, it was noticed that nickel in the Zircaloy-2 favored the absorption of hydrogen during reactor operation. The liberated hydrogen came from the corrosion reaction with water. When its concentration is extremely high in the cladding materials, zirconium hydride (ZrH_2) is precipitated, which reduces the ductility of the cladding [16].

$$ZrO_2 + H_2O \rightarrow ZrH_2 + \frac{3}{2} O_2 \qquad (2.1)$$

This situation was encountered in the early power plants that used Zircaloy-2 that contained nickel, responsible for the hydrogen up-take [17]. A new zirconium alloy with high corrosion resistance, strength, and ductility greater than Zircaloy-2 was fabricated and known as Zircaloy-3. This new alloy was developed not because of deficiency in the properties of Zircaloy-2, but by the desire to improve the corrosion resistance still further. The composition of Zircaloy-3 and Zircaloy-2 were almost the same, but the amount of tin in Zircaloy-3 was set at 2.5% as opposed to 1.5% for Zircaloy-2. The major difference between Zircaloy-2 and Zircaloy-3 was that Zircaloy-2 stringers were smaller in size; more uniformly distributed and contained fewer precipitates, $Zr(Cr, Fe)_2$ and $Zr_2(Ni,Fe)$ while Zircaloy-3 stringers were caused by a segregated grain boundary precipitate [11,18,19].

There was found to be a similarity between Zircaloy-2 and Zircaloy-3 in terms of water corrosion properties, and because it was found to be easy to minimize the appearance of stringers in Zircaloy-2, Zircaloy-3 was then abandoned due to its large size of stringers. The Zircaloy-2 composition was re-evaluated to produce two new Zircaloy alloys, Zircaloy-2 nickel - free and Zircaloy-4. The Zircaloy-2 nickel-free is primarily developed without the nickel addition. Zircaloy-4 is the other zirconium alloy, which contained the same chromium and tin levels as Zircaloy-2, but the iron content was increased to balance the removal of nickel. The difference between Zircaloy-2 and Zircaloy-4 is primarily due to nickel, which tends to absorb hydrogen so that Zircaloy-4 absorbs less hydrogen than Zircaloy-2 during high temperature water corrosion [15, 17]. Zircaloy-4 is used in pressurized light water reactor (PWR) applications and Zircaloy-2 is used in boiling water reactor (BWR) but has also, in Sweden, been tested in (PWR) environment [20].

Chapter 3

ALLOY PREPARATION

3.1. Introduction

Three rare earth-doped alloys have been prepared: zircaloy-4 alloys doped with 0.5 % Gd, 2.0 % Dy and 2.0 % Er. These are the maximum burnable poison concentrations in cladding expected for reaction application. These alloys were prepared by vacuum arc melting at Oak Ridge National Laboratory (ORNL). In addition, pure Zircaloy-4 was prepared using similar processing steps to serve as a control. These alloys were cold-rolled to 35 % reduction of area, the maximum thickness that was believed safe without experiencing cracking [21]. Intermediated anneals were used to prepare for the next stage of the rolling process. Five rolling steps were required to achieve a final thickness of approximately 1 mm (0.04 inch). Coupons were machined and exposed to superheated steam in an autoclave to test the corrosion resistance of the alloys. Tensile specimens were machined to obtain a quantitative measure of ductility. Scanning electron microscopy and energy dispersive x-ray analysis were performed to investigate the second phase formation and segregation of the rare earth elements in order to determine the mechanism of failure of the alloys.

3.2. Melting of Doped Alloys

Alloys were prepared from Zircaloy-4 (Teledyne Wah Chang Heat No. 242971) bars and inert gas arc melted to introduce the rare earth dopant. Zircaloy-4 bar was cut in

several pieces and weighted a total of 231 g. The alloy was then drop cast into a copper mold 60.2 mm (2.37 inches) long, 25.4 mm (1 inch) wide and 3.17 mm (0.125 inches) thick. Undoped Zircaloy-4 was also arc melted and cast in order to serve as control material. Approximately 297 g of Zircaloy-4 and 5.93 g of dysprosium were drop cast in the same ingot's size. The third melt was composed with 296 g of Zircaloy-4 and 5.92 g of erbium drop cast in a different mold 140 mm (5.5 inches) long, 25.4 mm (1 inch) wide and 9.52mm (0.375 inches) in thickness. Several samples of each ingot were obtained for chemical analysis, one each at the top, middle, and bottom of the gadolinium ingot and a single sample from each of the dysprosium and erbium ingots and then sent to an analytical laboratory for elemental analysis*. The results obtained confirm that the concentrations of the rare earth elements were nearly equal to the concentrations chosen for the absorbing elements. Table 3.1 shows the concentrations of the rare earths.

3.3 Alloy Fabrication

Three Zircaloy-4 based alloys were prepared, one doped with gadolinium, one doped with dysprosium and a third doped with erbium. Figure 3.1 is a flowsheet for a melt of a pure Zircaloy-4 that served as a control. Figure 3.2 shows a similar diagram for Zircaloy-4 doped with erbium, and Figures 3.3 and 3.4 show the processing of the dysprosium and gadolinium doped alloys, respectively. The alloys were rolled to 35% reduction of area using a maximum reduction of 10% per pass with several intermediate anneals. These sequences led to a fully recrystallized state.

*Galbraith Laboratories Inc.
P. O Box 51610, Knoxville, TN 37921 – 1700

The chemical composition of Zircaloy-4 used in this research is given in Table 3.2 [22].

Table 3.1: Summary of rare earth concentrations in Zircaloy-4 doped ingots

SAMPLE ID	RARE EARTHS	DESIRED CONCENTRATION. (WEIGHT %)	MEASURED CONCENTRATION (WEIGHT %)
18526-1 Ingot bottom	Gd	0.5	0.50
18526-2 Ingot top	Gd	0.5	0.49
18526-2 Ingot top	Gd	0.5	0.50
Zircaloy-4 Mold Ingot top	Gd	0.5	0.49
18527-1 Ingot bottom	Gd	0	<0.03
18184-1 Ingot top	Dy	2	1.80
18785-1 Ingot top	Er	2	1.83

Table 3.2: Chemical Composition of Zircaloy-4 (Wah Chang Heat No 242971)*

Main Element Composition	Element Weight Percent
Sn	1.28
Fe	0.22
Cr	0.12
Fe + Cr	0.34
O	0.13
Ingot Element Impurity	**Element in ppm**
Al	41
B	0.30
C	161
Ca	<10
Cd	<0.25
Cl	<5
Co	<10
Cu	<25
H	<3
Hf	53
Mg	<10
Mn	<25
Mo	<10
N	27
Na	<5
Nb	<50
Ni	<35
P	8
Pb	<25
Si	97
Ta	<100
U	<1
V	<25
W	<50

*Wah Chang
P. O Box 460, Albany, Oregon 97321 – 0136

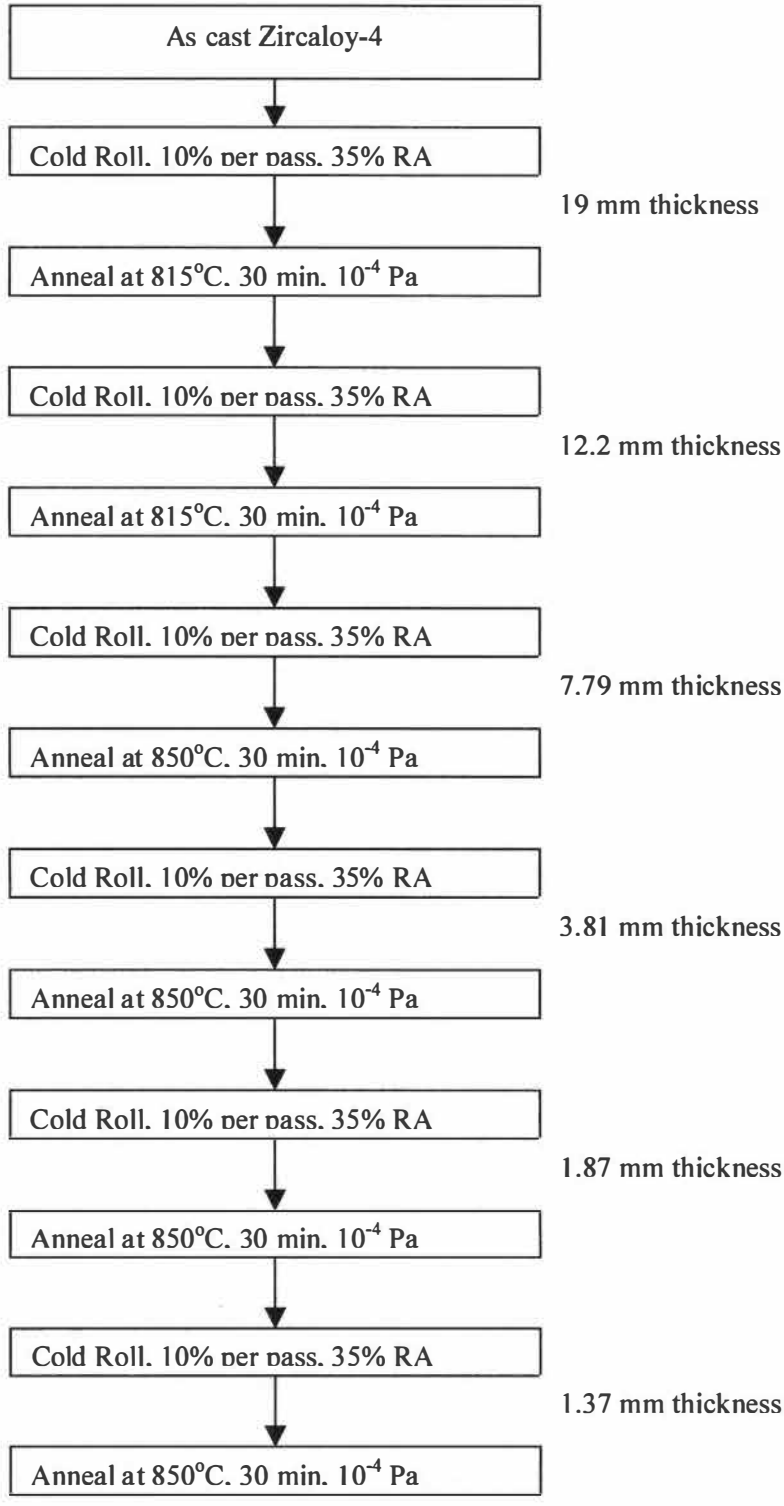

Figure 3.1: Simplified flowsheet of undoped Zircaloy-4 prepared by arc melting in an inert atmosphere and cast into an ingot and cold rolled to about 1 mm

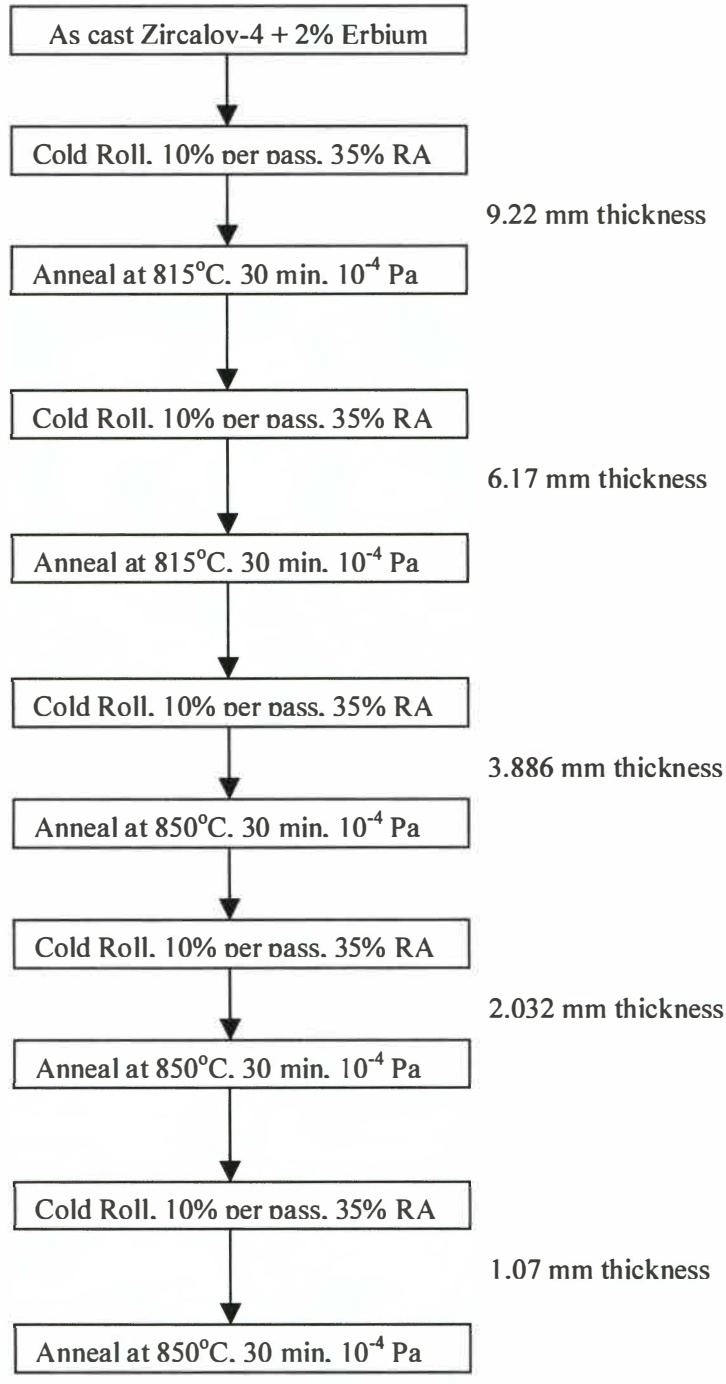

Figure 3.2: Simplified flowsheet of Zircaloy-4 doped with 2% erbium prepared by arc melting in an inert atmosphere and cast into an ingot and cold rolled to about 1 mm

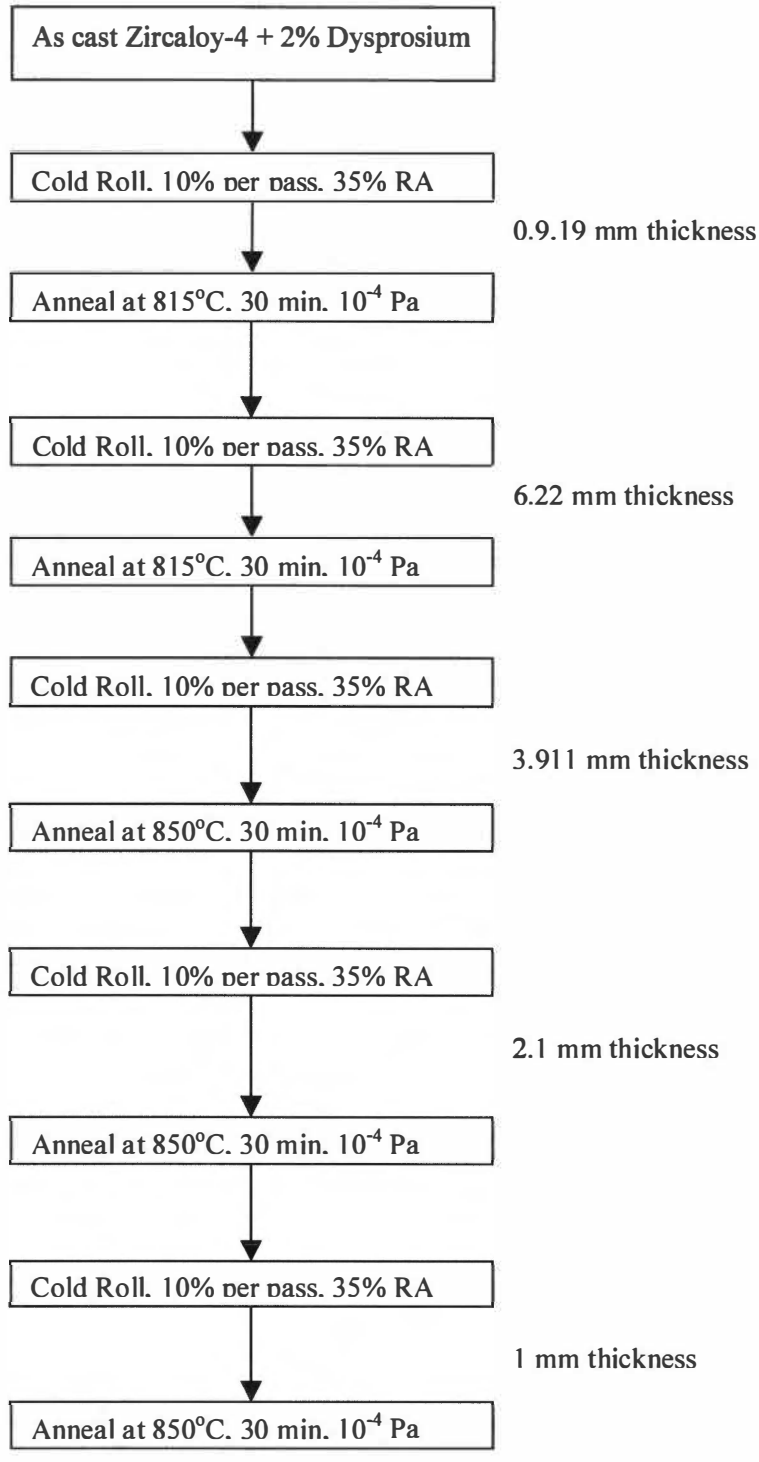

Figure 3.3: Simplified flowsheet of Zircaloy-4 doped with 2% dysprosium prepared by arc melting in an inert atmosphere and cast into an ingot and cold rolled to about 1 mm

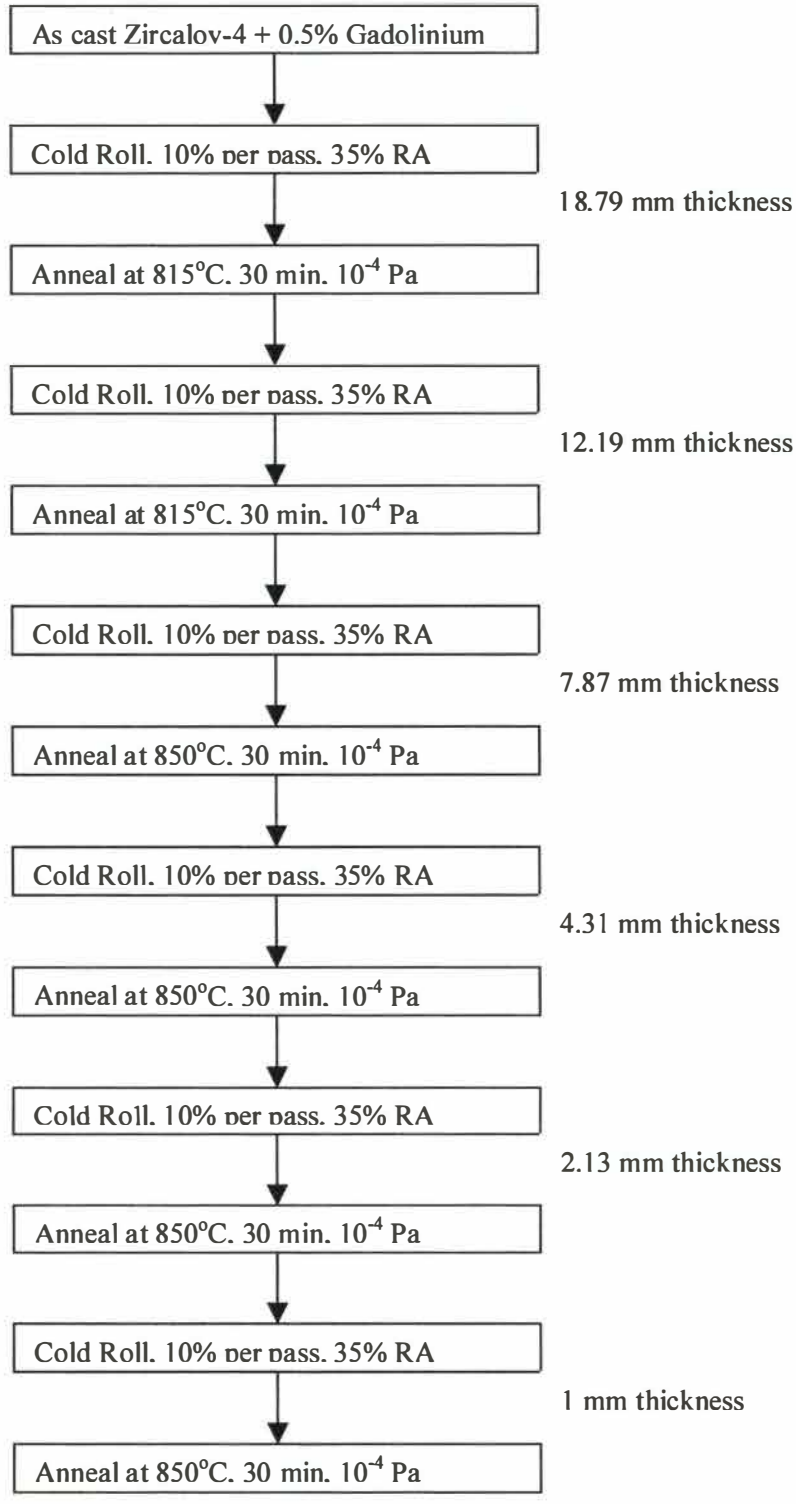

Figure 3.4: Simplified flowsheet of Zircaloy-4 doped with 0.5% gadolinium prepared by arc melting in an inert atmosphere and cast into an ingot and cold rolled to about 1 mm

Chapter 4

CORROSION OF ZIRCONIUM ALLOYS

4.1. Introduction

Of the properties that can be affected by doping Zircaloy-4 with rare earths, ductility, strength, and corrosion behavior are the most likely to be degraded. To investigate corrosion, it was decided to perform a high temperature steam exposure test in an autoclave. ASTM G2, 1996, G2-88 (Reapproved 2002) [Standard Test Method for Corrosion Testing of Products of Zirconium, Hafnium, and Their Alloys in Water at 360°C (680°F) or in Steam at 400°C (750°F)] was used to test the specimens. According to this standard, the test is primarily used as an acceptance test for products of zirconium, hafnium, and their alloys. This standard has been widely used in the development of new alloys, heat treating practices, and evaluating of welding techniques. It was decided to use steam at 400°C for a period of 14 days.

4.2. Fabrication and Specimen Description

The rare earth doped Zircaloy-4 sheets described in chapter 3 were machined into coupons. Subsequently, all specimens were chemically etched, thoroughly cleaned and carefully rinsed to prepare the surfaces for testing in order to eliminate the effects of machining. It is necessary to produce a smooth shiny surface free of stains, as specified in ASTM G2-88 [Standard Test Method for Corrosion Testing of Products of Zirconium, Hafnium and Their Alloys in Water at 360°C (680°F) or in Steam at 400°C (750°F) [25,

26]. Four replicate specimens of each alloy were supplied to Battelle Columbus Laboratory* for testing. Each specimen was approximately 1.4 mm thick, 50 mm wide, and 20 mm long. A hole having a nominal diameter of 3.2 mm had been drilled on one end of each specimen for hanging on a support fixture. Specimens prior to autoclave testing are depicted in Figure 4.1 [23].

4.3. Autoclave Testing

Immediately prior to testing, the specimens were again thoroughly cleaned, wiped with reagent grade acetone and ethanol and then weighed with an analytical balance to a precision of 0.01 mg. Upon weighing, the specimens were hung on a quartz fixture designed to hold the specimens during the autoclave operation. A 250 ml charge of distilled water with a resistivity of 18 M-ohm-cm was placed in a one-liter autoclave along with the specimens and holder. Figures 4.2 and 4.3 show photographs of a quartz specimen holder and a top view of the specimens in situ [23]. The specimens were exposed to high-temperature steam in an autoclave for 336 hours at 400°C (750°F) according to ASTM G2-88 (Reapproved 2002). The pressure of the autoclave was maintained at 1,500 Psi during the entire operation. The specimens were removed and then weighed to determine the weight gained.

---

*Battelle Columbus Laboratory
Columbus, Ohio 43201 – 2693

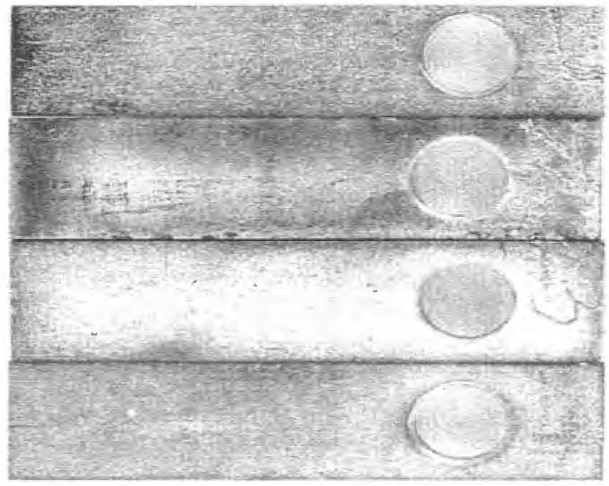

Figure 4.1: Photograph of pure zirconium specimens prior to testing

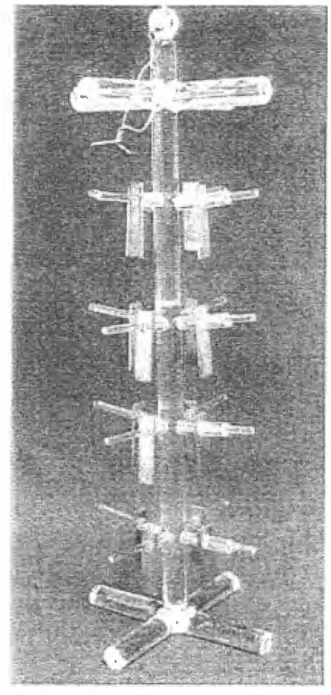

Figure 4.2: Photograph of the quartz specimen holder and the zirconium specimens prior testing

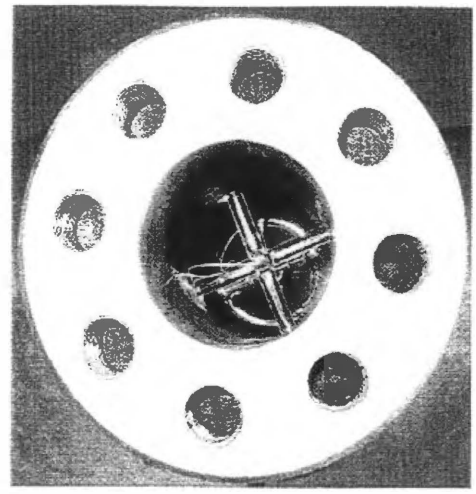

Figure 4.3: Photograph of top of autoclave holding specimen holder and water

4.4. Autoclave Performance Results

Undoped Zircaloy-4 survived the test, as expected, and exhibited the measured mean mass gain of 1.07 g per square meter which agrees with the mass gain found in the round robin tests listed in ASTM G2 within about a factor of two [24]. From this result, one can conclude that coupons of pure Zircaloy-4 were corroded because corrosion rates are measured as weight gains rather than weight losses since the oxide film cannot be removed easily. On the other hand, the Zircaloy-4 doped with gadolinium revealed a weight loss. During the autoclave test, some of the alloy ingredients will disappear or partially disappear and lead to the degradation of metal caused by a reaction with the environment, such as oxidation and chemical attack of the metallic surface resulting in a failure of the specimen. Anderson reported that, "All zirconium alloys react with water to form the corrosion product zirconium dioxide and hydrogen" [11].

The anodic reaction can be written as follows:

$$Zr\ (m) \longrightarrow Zr^{+4}(aq) + 4e^{-} \quad (4.1)$$

The cathodic reaction may be:

$$H_2O + H^{+} + 2e^{-} \longrightarrow H_2\ (g) + OH^{-} \quad (4.2)$$

$$Zr^{+4}(aq) + 4OH^{-} \longrightarrow Zr\ (OH)_4\ (aq) \quad (4.3)$$

This result can be supported by the fact that formation of a passive film on surface of the Zircaloy-4 alloys in an oxidation process. The growth of the film is partially determined by the migration of the zirconium ions provided in Equations 4.1 and 4.2 [27]. In the case of Zircaloy-4 doped with 0.5% Gd, it is apparent that oxide did not form a stable tenacious layer as evidenced by the loss of metal. Two of the doped alloys failed to pass the corrosion test. Zircaloy-4 doped with erbium and Zircaloy-4 doped with dysprosium turned to powder. Scanning electron microscopy (SEM) and energy dispersive x-ray (EDX) were used to conduct an investigation to determine the failure of these two alloys. Figure 4.4, shows the powder collected from the bottom of the autoclave. The powder is composed of fine and large particles. Table 4.1 shows the results of corrosion testing.

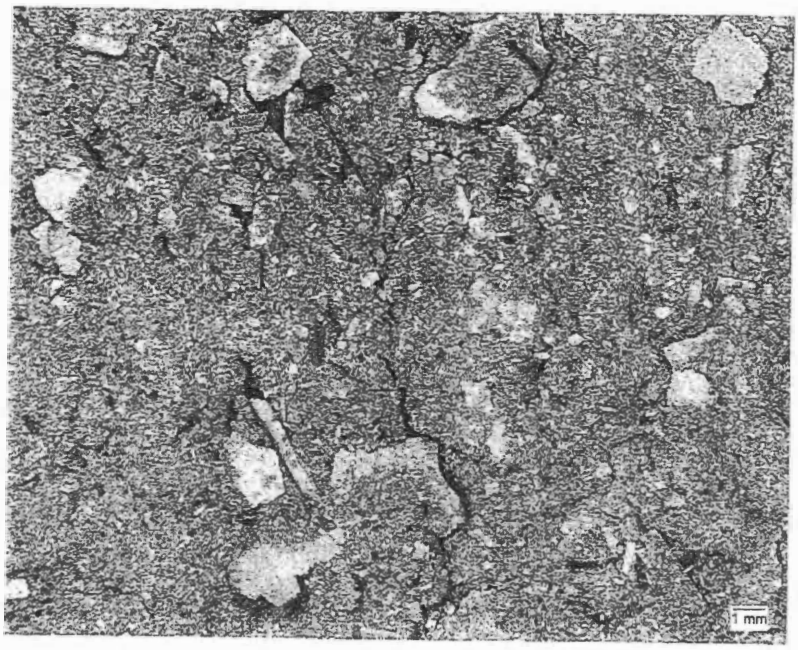

Figure 4.4: Powder remnants of the zirconium alloys destroyed during autoclave testing

Table 4.1: Summary of weight changes before and after autoclave corrosion testing

Alloy	Sample	As-received Weight (g)	Cleaned Weight (g)	Post-test Weight (g)	Weight Change (g)	Mass gain (g/m^2)
Zr 100 %	Z-1	0.81908	0.81905	0.82198	0.00293	1.10
	Z-2	0.81310	0.81308	0.81560	0.00252	0.94
	Z-3	0.81500	0.81498	0.81779	0.00281	1.05
	Z-4	0.81198	0.81192	0.81508	0.00316	1.18
					Mean:	1.07
					Std dev:	0.10
Zr+0.5%Gd	G-1	0.61502	0.61498	0.61370	-0.00128	-0.479
	G-2	0.61618	0.61614	0.61486	-0.00252	-0.479
	G-3	0.61178	0.61172	0.60737	-0.00435	-1.629
	G-4	0.61462	0.61456	0.61097	-0.00359	-1.345
Zr + 2% Er	E-1	0.56289	0.56282	No data available		
	E-2	0.56968	0.56954			
	E-3	0.56667	0.56658			
	E-4	0.57105	0.57097			
Zr + 2% Dy	D-1	0.58896	0.58894	No data available		
	D-2	0.58919	0.58913			
	D-3	0.59091	0.59088			
	D-4	0.58328	0.58323			

Chapter 5

MICROSTRUCTURES OF ZIRCONIUM ALLOYS

5.1. Optical Microscopy

The optical microscope is the most important tool currently used in the analysis of microstructures. It is used together with scanning and transmission electron microscopes in order to examine the microstructure of metals, noting the effects of alloying elements, plastic deformation, including heat treatments. The microscope is built of two distinct and separate optical systems: the objective and the eyepiece. It differs from the biological-type microscope in that reflected light rather than transmitted light is used. The total magnification is based upon the size of the virtual image relative to the object. The virtual image appears to exist at 250mm, which is the closest distance from the eye at which a normal-sighted person focuses with maximum eye accommodation [28].

5.2. Specimen Preparation for Light Microscopy

Three perpendicular surfaces of each alloy were prepared for viewing using conventional metallographic techniques. Due to the expected unstable nature of the microstructures, samples for further examination were prepared by electropolishing. To obtain the microstructures that characterize the Zircaloy-4 morphological features, samples were polished at Oak Ridge National Laboratory, using the Struers* polishing

---

*Struers Inc.
Cleveland, OH 44145

Equipment and abrasive products using the following procedure:

- 5 minutes: Dp-Allegro Disc:Dp-Lub (drip): 6 micron suspension
- 5 minutes: Dp-Largo Disc:Dp-Lub (drip): 6 micron suspension
- 5 minutes: Dp-Dac cloth: Dp-Lub (drip): 3 micron suspension
- 5 minutes: Dp-Nap cloth: Dp-Lub (drip): 1 micron suspension

The samples were etched for less than one minute in a mixture of 50% water, 20% hydrofluoric acid, 10% nitric acid and 20% sulfuric acid [29]. Optical metallography was performed to determine any change in microstructure or precipitate morphology after the addition of rare earth elements.

5.3. Optical Microstructural Analysis

The interpretation of the microstructure of metals and alloys is the most important tool available in examining the effects of mechanical, thermal, and chemical treatments. Adding another element to a pure metal to form a solid solution does not usually change the microstructure in an obvious manner, but the mechanical and physical properties are modified completely [30,31].

The first examination was to view the general morphology and determine grain size. The grain structure is shown in figures 5.1-5.4. Grain size was determined by the line intercept method in ASTM E-112-96, Standard Test Methods for Determining Average drain size. Magnification was determined using a standard scale with 0.01 mm graduations. Figure 5.1 represents the microstructure of undoped annealed Zircaloy-4 at

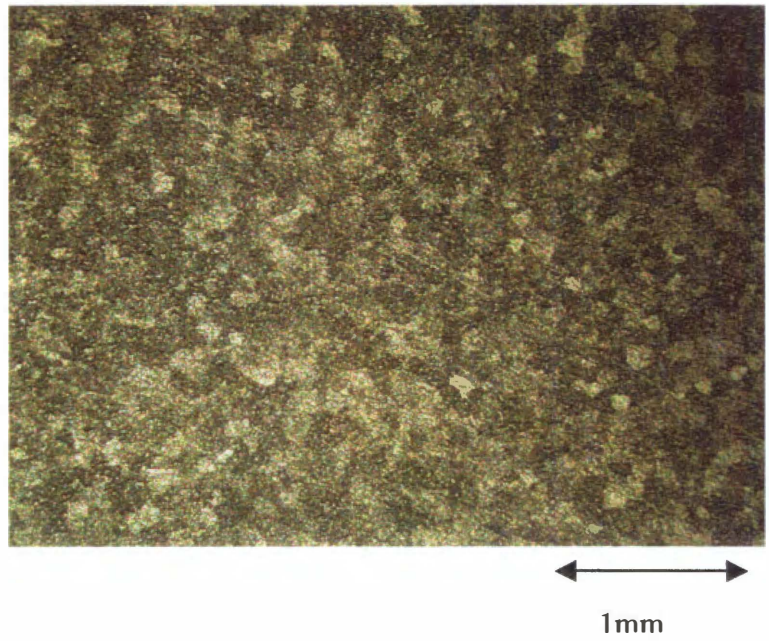

Figure 5.1: Pure Zircaloy-4 after annealing at 850°C/ 30 minutes

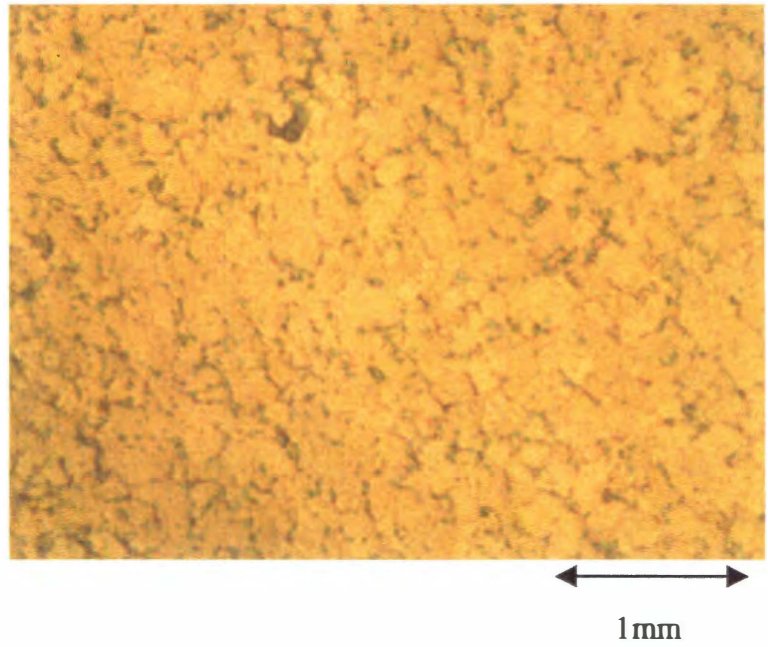

Figure 5.2: Zircaloy-4 doped with 0.5 % gadolinium after annealing at 850°C/30 minutes

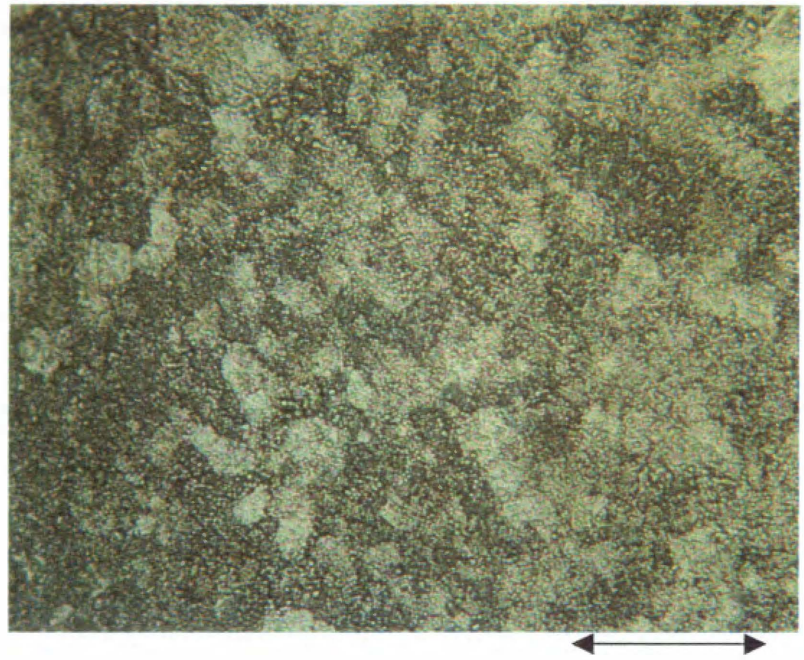

Figure 5.3: Zircaloy-4 doped with 2% dysprosium after annealing at 850°C/ 30 minutes

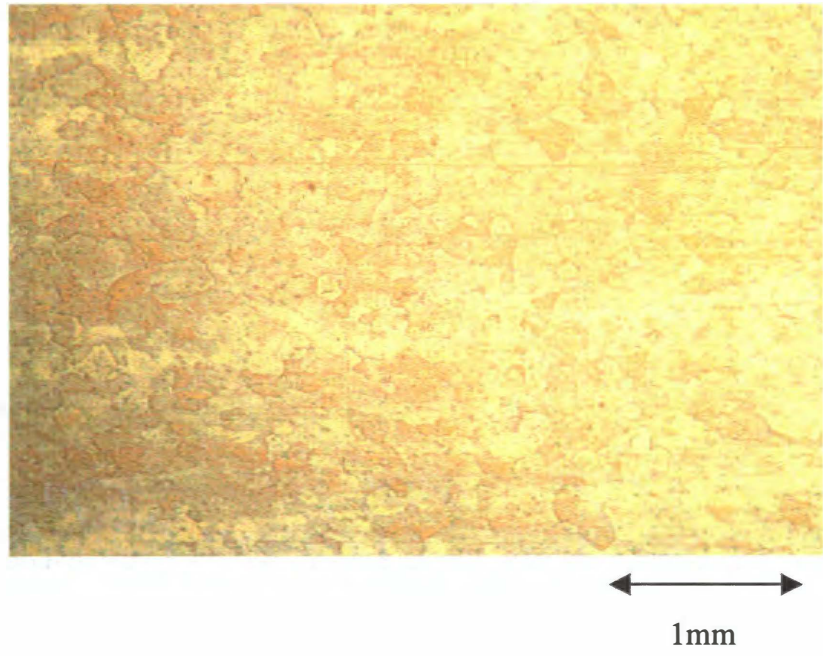

Figure 5.4: Zircaloy-4 doped with 2% erbium after annealing at 850°C/ 30 minutes

220x. The grains appear uniform and equiaxed. Small precipitates expected to be of Zr $(Cr,Fe)_2$ and Zr_2 (Ni,Fe) appear within the grains. The grain size was determined to be 6 μm, ASTM grain size 8. Figure 5.2, shows the microstructure of Zircaloy-4 doped with 0.5% gadolinium annealed at a temperature of 850 °C for 30 minutes. It revealed uniform grain size with grain boundaries decorated with precipitation at a magnification of 220x. The average grain size of 6 μm is similar to unalloyed Zircaloy-4. The nature of these precipitates remains to be determined by further analysis. The micrograph of Zircaloy-4 doped with 2% dysprosium annealed at 850°C for 30 minutes is shown in Figure 5.3. After examining the microstructure at magnification of 220x, the grain size of 6μm was determined, in agreement with that of undoped Zircaloy-4. Although grain size was similar to that of undoped Zircaloy-4, there appears to be larger precipitates. Figure 5.4 shows the microstructure of Zircaloy-4 doped with 2% erbium with fine equiaxed grains with an average grain size of 6 μm. The shape and size of grains turned out to be heterogeneous when compared to the control.

5.4. Scanning Electron Microscopy

In order to reveal more detail, scanning electron microscopy (SEM) was used to examine the specimens. There are several reasons for using the SEM rather than other instruments. Bindell reports that the SEM provides the investigator with a highly magnified image of the surface of a material that is very similar to what one would expect if one could actually see the surface visually [28]. It is also capable of being operated with a large depth of field, which permits a large amount of the sample to be in focus at

one time. Furthermore, the SEM generates micrographs of high resolution, which reveal closely spaced features, which may be analyzed at a high magnification. With these advantages, the SEM is capable of generating good images that represent the three-dimensional sample. In addition, an energy dispersive x-ray spectrometer is used to determine the elemental concentration in a microvolume of sample. The SEM used for this investigation (Carl Zeiss model 1525)* has a resolving power of 2 nm and a magnification of over 500,000x while a modern light microscope has a magnification of approximately 1000x and a resolution of 0.02μm [32].

5.4.1. Sample Preparation

It is relatively easy to conduct an analysis of the internal structure of zirconium alloys using a scanning electron microscope (SEM) since it requires very little in terms of sample preparation. In addition, a metallic sample is conducting so that charge build-up on the surface of the specimen is avoided. The specimen must be vacuum compatible and must fit into the specimen chamber [28]. Most of the specimens examined were epoxy-mounted specimens already prepared for light microscopy. Since the samples were epoxy mounted, a copper foil was placed on top of the sample to conduct a current to the stage ground. The combination of higher magnification, greater resolution, larger depth of field, and ease of sample preparation makes the SEM one of the most sophisticated desirable instruments for many research areas [32].

---

*Carl Zeiss
Thornwood, New York 10594

The high-energy electrons in the beam of the SEM eject low level, k and l electrons from elements of the target. Characteristic x -rays resulting from the cascade of higher-level electrons to fill the vacant states permits identification of the elements in the sample. This is known as energy dispersive x-ray analysis (EDX).

The powder residue from the autoclave was examined to determine if the sample failed along grain boundaries and if segregation of the dopant elements produced failure. Figure 5.5 shows SEM micrographs of powder collected on the bottom of the autoclave, after autoclave exposure for 336 hours. The powder was composed of large and small chips of Zircaloy-4 doped with erbium and dysprosium. Examination with energy dispersive x-ray (EDX) directing the beam on random particles showed both Zircaloy-4 constituents and dopant elements, but no segregation was detected. A representative composition is shown in Table 5.1, and the corresponding energy spectrum is shown in Figure 5.6. A large particle was found fractured in two pieces, shown in 5.7. The energy dispersive x- ray (EDX) spectrum, Figure 5.8, and corresponding composition, Table 5.2 again reveals no segregation. Energy dispersive x-ray was also conducted randomly on a large particle of the powder collected after the autoclave testing. Figures 5.9 through 5.12 show the EDX spectrums and SEM micrograph and Tables 5.3 through 5.6 present EDX compositions conducted on bright and dark areas. The tables also represent information of small particle and the second part of large particle. Again, these tables and figures reveal no segregation of rare earths along grain boundaries.

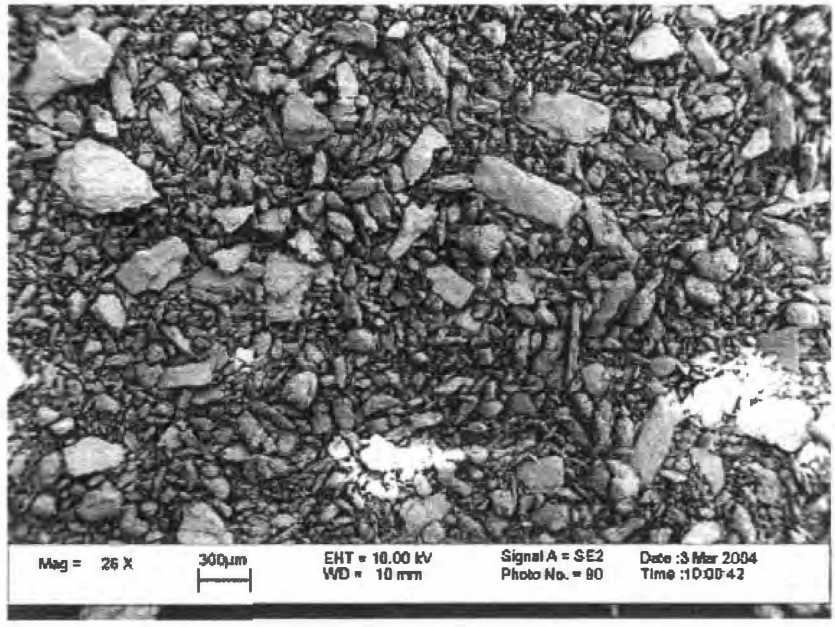

Figure 5.5: SEM micrograph of fine powder collected from the bottom of the autoclave.

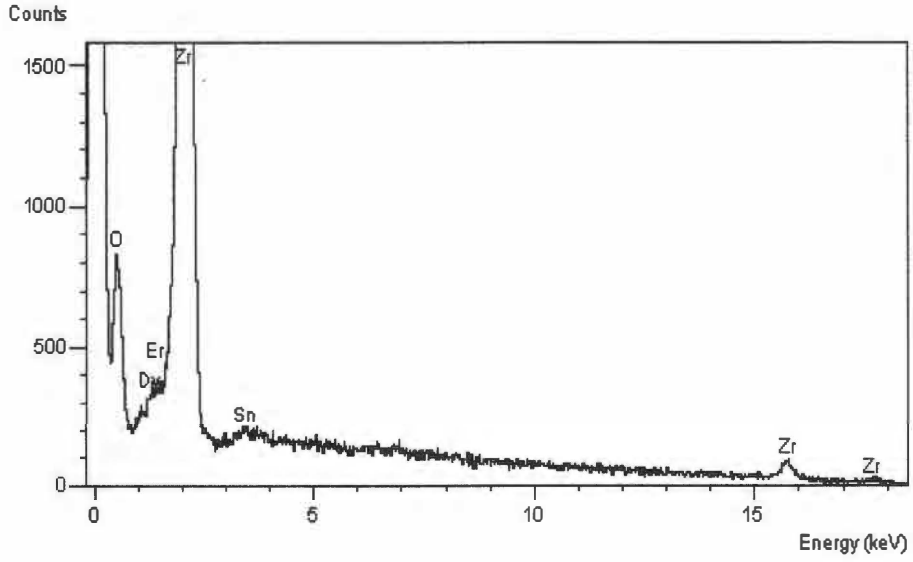

Figure 5.6: EDX spectrum of fine powder collected at the bottom of the autoclave test

Table 5.1: EDX compositional analysis of fine powder collected at the bottom of the autoclave

ELEMENT	ELEMENT WEIGHT %	ATOMIC %
O	44.40	82.21
Zr	53.46	17.36
Sn	0.61	0.15
Dy	0.59	0.11
Er	0.93	0.17
Total	100.00	100.00

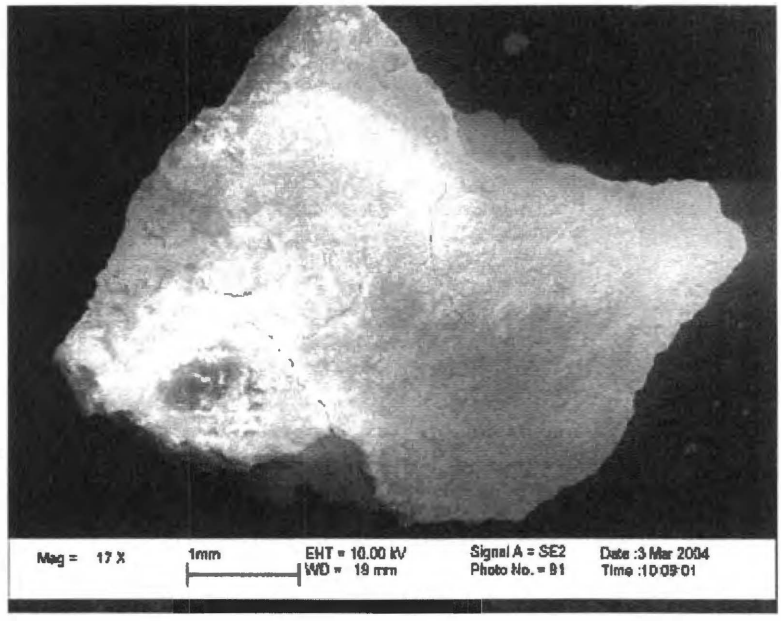

Figure 5.7: SEM micrograph of large particle found in the powder collected from the bottom of the autoclave

Table 5.2: EDX compositional analysis on large particle found in the powder collected at the bottom of the autoclave

ELEMENT	ELEMENT WEIGHT %	ATOMIC %
O	51.01	85.68
Zr	47.99	14.14
Sn	0.29	0.07
Dy	0.71	0.12
Total	100.00	100.00

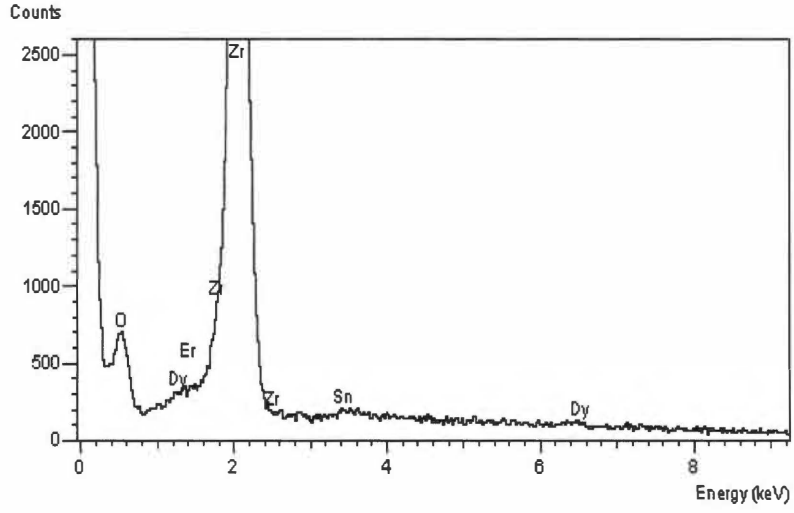

Figure 5.8: EDX spectrum on dark area of large particle of the collected powder after autoclave test

Table 5.3: EDX compositional analysis on dark area of large particle of the collected powder after autoclave test

ELEMENT	ELEMENT WEIGHT %	ATOMIC %
O	47.81	84.05
Zr	50.84	15.68
Sn	0.68	0.16
Dy	0.67	0.12
Total	100.00	100.00

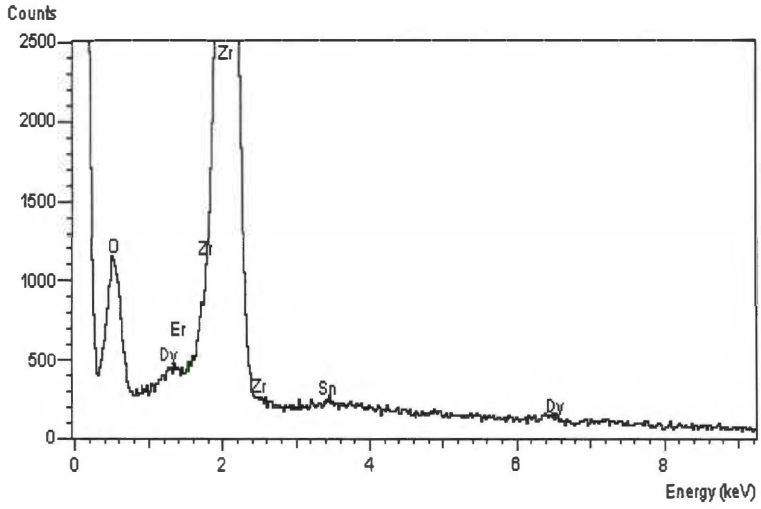

Figure 5.9: EDX spectrum on bright area of large particle of the collected powder after autoclave test

Table 5.4: EDX compositional analysis on bright area of large particle of the collected powder after autoclave test

ELEMENT	ELEMENT WEIGTH %	ATOMIC %
O	49.68	85.07
Zr	48.49	14.56
Sn	0.89	0.20
Dy	0.95	0.16
Total	100.00	100.00

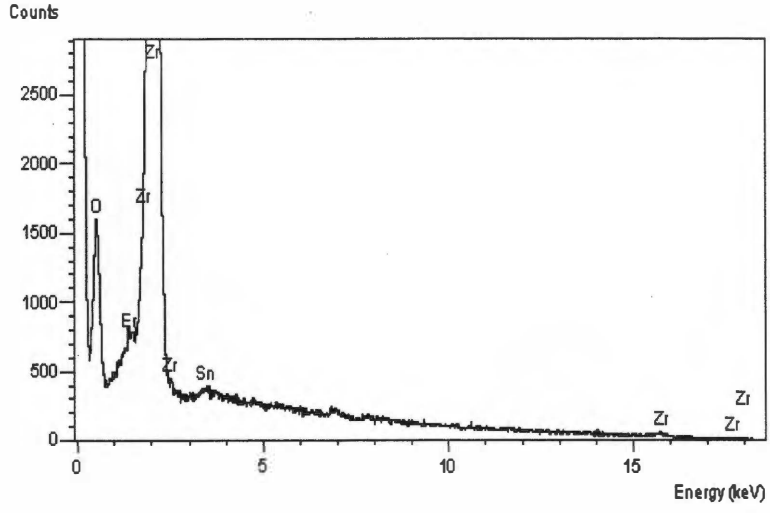

Figure 5.10: EDX spectrum on small particle found in collected powder after autoclave test

Table 5.5: EDX compositional analysis on small particle found in collected powder from the bottom of autoclave

ELEMENT	ELEMENT WEIGHT %	ATOMIC %
O	49.99	85.23
Zr	48.36	14.46
Sn	0.57	0.13
Er	1.08	0.18
Total	100.00	100.00

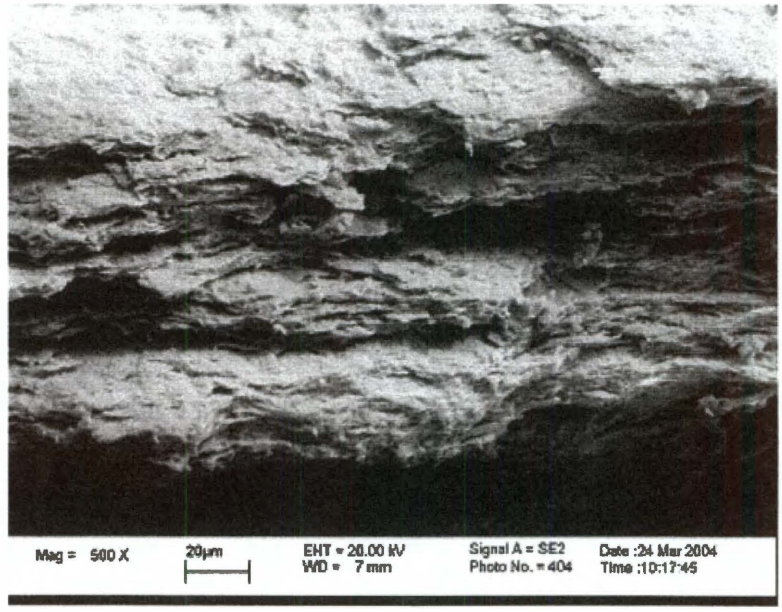

Figure 5.11: SEM micrograph on fracture surface of the left part of large particle of powder collected from the bottom of the autoclave

Table 5.6: EDX compositional analysis on fracture surface of the left part of large particle of powder collected from the bottom of autoclave

ELEMENT	ELEMENT WEIGHT %	ATOMIC %
O	38.54	78.33
Zr	59.55	21.23
Sn	0.78	0.21
Dy	1.13	0.23
Total	100.00	100.00

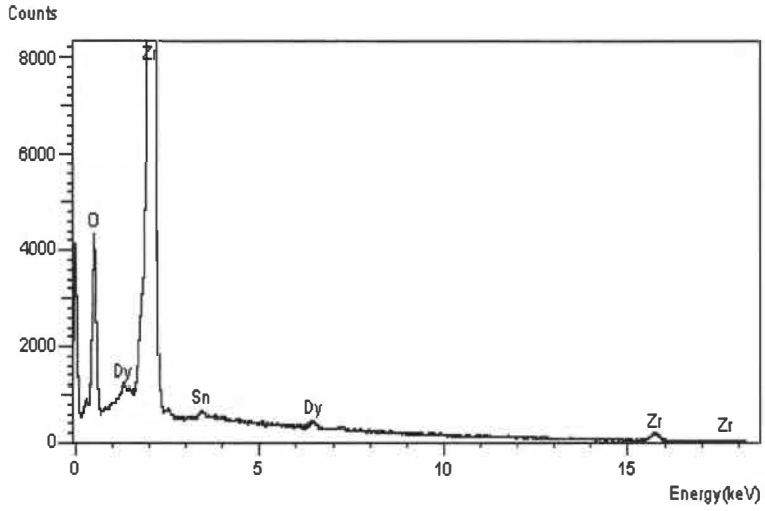

Figure 5.12: EDX spectrum of fracture surface of the left part of a large fractured particle of the powder collected on the bottom of the autoclave

Chapter 6

TENSILE TESTS

6.1. Introduction

The tensile test is the most widely used mechanical property test. The purpose is to measure strength and ductility. This experiment is based on the America Society for Testing and Materials (ASTM) standard tensile test. In this project, metallic rare earth elements, serving as burnable poisons are alloyed with Zircaloy-4 rather than mixed with fuel in the form of compounds. The effect of such additions on the ductility is the subject of interest. The tensile loads are applied to a specimen, which has an approximate area of 0.0322 cm^2 (0.0050 square inches) and a gauge length of 12.7 mm (0.5 inch). The applied axial loads and the corresponding deformation are measured, and stresses and strains are also determined. In addition, a stress-strain plot is developed from the stress and strain data, which exhibits important information about the mechanical properties.

Another key objective of this experiment is to identify the failure mechanism through analysis of fracture surfaces. Fractography, as the technique is called, was used to determine the failure origin, direction of crack propagation, failure mechanism, material defects, environmental interaction, and the nature of stresses [33]. Once again, scanning electron microscopy (SEM) was used to perform the fracture surface analysis. Energy dispersive x-ray analysis was again used to investigate elemental segregation and precipitation.

6.2. Background

The design performance of a product depends on mechanical properties of a material and its capacity to resist deformation under stress. The tensile test is the most fundamental type of mechanical test that one can perform to characterize the mechanical properties of materials. This test uses a machine that applies and measures force or load at constant strain rate. Generally, an extensometer or strain gauge is attached to a gauge section on the test specimen to measure the axial elongation, but this is not necessary to obtain useful data. A strain gauge load cell in the load train monitors the specimen load. The gauge length and initial cross sectional area are obtained from measurement of the test specimen. Strain, ε, is defined by

$$\varepsilon = \frac{l_f - l_0}{l_0} \tag{6.1}$$

where,

l_0 = The initial gauge length

l_f = The final gauge length

The stress is computed from the expression

$$\sigma = \frac{F}{A_0} \tag{6.2}$$

where,

F = Tensile load being applied to the specimen

A_0 = Initial cross-sectional of the gauge section

This is known as the engineering stress, based upon the original area rather than upon the instantaneous area which is used to compute the true stress, another useful quantity. A stress-strain curve is developed when force-elongation data are converted to stress and strain. It is more preferable to deal with the stress-strain curve rather than force versus elongation due to its dependency on specimen dimensions. The point of maximum stress is typically called ultimate tensile strength or UTS on the plot. It is computed as follows:

$$UTS = \frac{F_{max}}{A_0} \tag{6.3}$$

where,

F_{max} = Maximum tensile stress

A_0 = Initial cross-sectional area of the gauge section

After the point of maximum load has been reached, the gauge section is no longer uniformly strained. Deformation is mostly confined to a localized region of necking of the specimen.

There are three parameters that are used to characterize the ductility of a material. First, the total elongation is defined as follows

$$TE = \frac{(l_f - l_0)}{l_0} \tag{6.4}$$

where,

l_0 = The initial gauge length

l_f = The final gauge length

TE = Total elongation

$$RA = [\frac{A_0 - A_f}{A_0}] \tag{6.5}$$

where,

A_0 = Initial cross-sectional of the gauge section

A_f = Final cross-sectional of the gauge section

RA = Reduction of area

$$UE = (\frac{l_U - l_O}{l_O}) \tag{6.6}$$

l_U = the elongation at maximum load

Uniform elongation (UE) is an additional measure of ductility and is the ductility up to the point where uniform deformation breaks down.

When performing the tensile testing, the initial stage of the test is characterized by elastic deformation where the relationship between the applied load and elongation of the specimen is linear. In this region, the ratio of stress and strain is constant and computed as follows [31]:

$$E = \frac{\sigma}{\varepsilon} \tag{6.7}$$

where,

σ = Stress

ε = Strain

E is the slope of the line and called Modulus of Elasticity or Young Modulus, which is a measure of stiffness of the material. At the point that the curve is no longer linear and

deviates from the straight line, plastic or irreversible, deformation starts to occur. This point is defined as the elastic limit where there is a gradual transition from elastic to plastic behavior. In the USA, the yield strength or offset yield strength is a more commonly measured parameter and is set as the stress at a plastic strain of 0.2% [31].

$$Stress = \frac{F_{(Strain-Offset=0.002)}}{A_0} \tag{6.8}$$

Typical behavior is shown in Figure 6.1. The linear region exists up to point A, which is known as elastic limit or proportional limit. Beyond the proportional limit, the yield stress is reached, where the plastic strain is equal to a pre-defined value, 0.2%. Beyond point C, where the force is maximum, the specimen begins to deform non-uniformly and necking begins. The specimen can no longer strengthen by deformation, and the load supported decreases until rupture at point D. As an elastic and plastic deformation curve illustrates, Figure 6.2 presents a visual description of stress-strain behavior where the circular insets represent the geometry of the deformed specimen at different points along the curve described in Figure 6.1 [31].

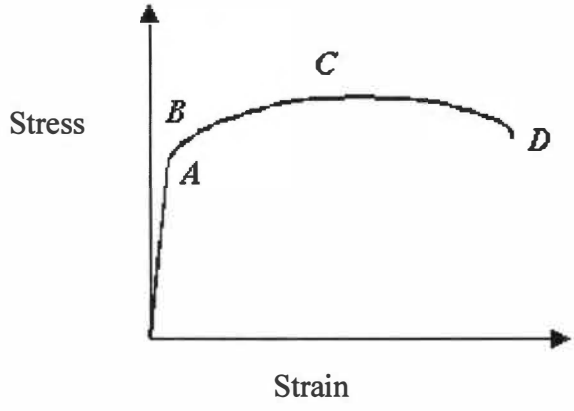

Figure 6.1: Schematic of elastic and plastic deformation

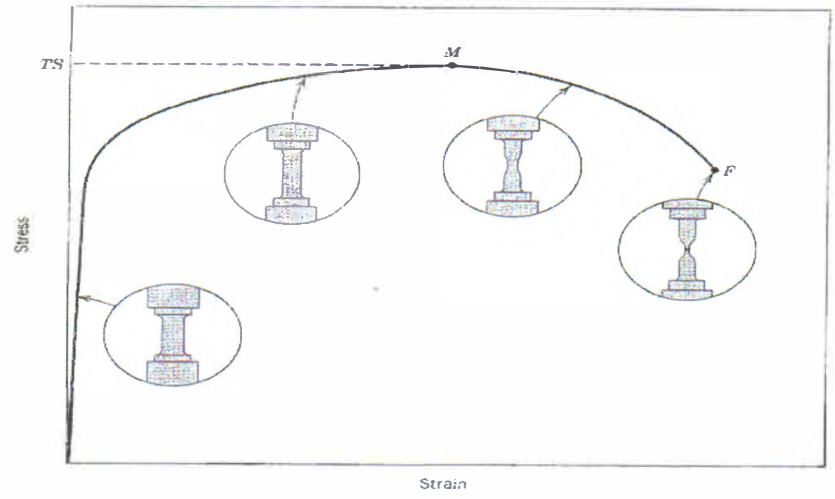

Figure 6.2: Visual description of engineering stress- strain behavior to fracture point F

6.3. Tensile Specimen Design

The same sheet that was used for the corrosion test coupons was used for tensile testing. The specimens were stamped from the sheets that were used in the annealed condition and accommodated the testing mechanism that uses a loading shoulder to apply the necessary force. Each specimen was composed of a pair of shoulder ends, illustrated in Figure 6.3, which provided the point of contact between the specimen and the testing mechanism.

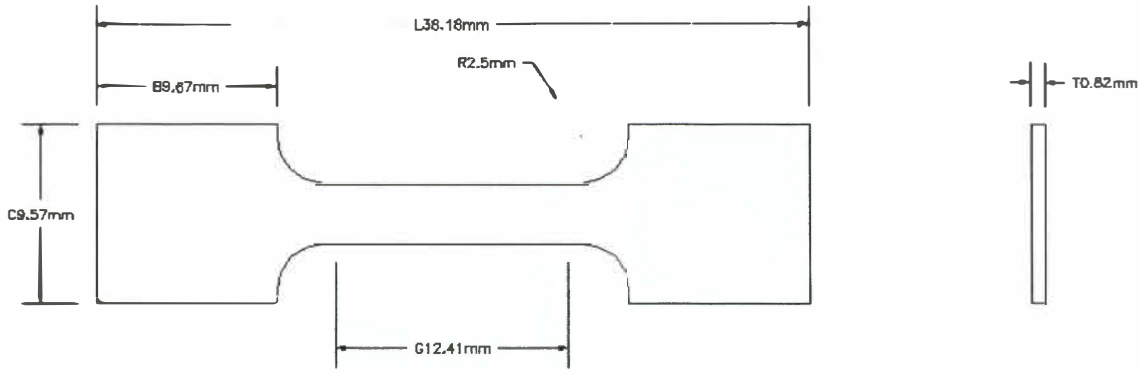

Figure 6.3: Schematic of tensile testing specimen

Tensile tests were conducted at room temperature at a strain rate of 6.67E-4s^{-1} by using a MTS* model, servo-hydraulic testing machine, which may be used for both tension and compression testing. The maximum load capacity of the load frame was 25,000 kg (55,115.5 lb) and 65,000 lbf load cell was used. The type of grip used for this experiment is called a shoulder grip, designed at the University of Tennessee Knoxville Machine Shop. A total of 4 specimens from each alloy including undoped Zircaloy-4 were tested.

---

*MTS Systems Corporation,
Eden Prairie, MN 55344-2290

6.4. Results and Discussion

6.4.1. Tensile Testing

An extensometer was not fastened to the specimen; however extension was measured by a linear variable differential transformer, LVDT, attached to the pull rod. This results in recording deformation of the load train and the machine itself, but this unwanted deformation was subtracted out. Figure 6.4 a presents a typical curve from a tensile test of undoped Zircaloy-4. This plot was developed from Figure B-1 that is shown in appendix B. Figure A-2 in appendix A also presents tensile test results for free Zircaloy-4 of specimen 3. Since these specimens were tested without an extensometer attached to the gauge length, the elastic portion of the curve is not meaningful. Because of this, a handbook value for Young's Modulus was used to draw the elastic portion of the curve in Figure 6.4 and the other tensile curves presented in this section. A value of 98 GPa for pure Zircaloy-4 reported in [10] was used to construct the linear portion of the curve. Corresponding curves for the doped alloys are shown in Figures 6.5-6.7. It can be observed in Table 6.1 that the undoped Zircaloy-4 specimens have both shown lower ductility, ultimate tensile strength and yield strength than the basic mechanical properties reported by Bertolino, Meyer and Ipina [32] who observed 522 MPa ultimate tensile strength, 365 MPa yield strength and 27.8% elongation for mechanical properties of Zircaloy-4 at room temperature. The total elongations reported in table 6.1, are almost in agreement with that of 18% for unirradiated guide tube specimens at room temperature and 22% for unirradiated cladding specimens at 300°C (572°F) reported by Yagnik, Rashid and Yang [35]. The uniform elongations reported in Table 6.1, are close

Table 6.1: Mechanical properties of the Zircaloy-4 alloys

Tensile Properties	Undoped Zircaloy-4		Erbium doped		Dysprosium doped			Gadolinium Doped		
Samples	Zr-1	Zr-3	Er-1	Er-2	Dy-1	Dy-2	Dy-3	Gd-1	Gd-2	Gd-3
Yield Strength (MPa)	394	379	331	366	456	455	462	414	428	392
Ultimate Tensile Strength (MPa)	461	461	428	468	526	524	537	497	517	455
Total Elongation (%)	21	20	25	24	23.3	22	23	16.6	18.5	10.8
Uniform Elongation (%)	7.6	9.2	8.64	8.4	8.84	8.0	7.68	7.4	10.4	4.3

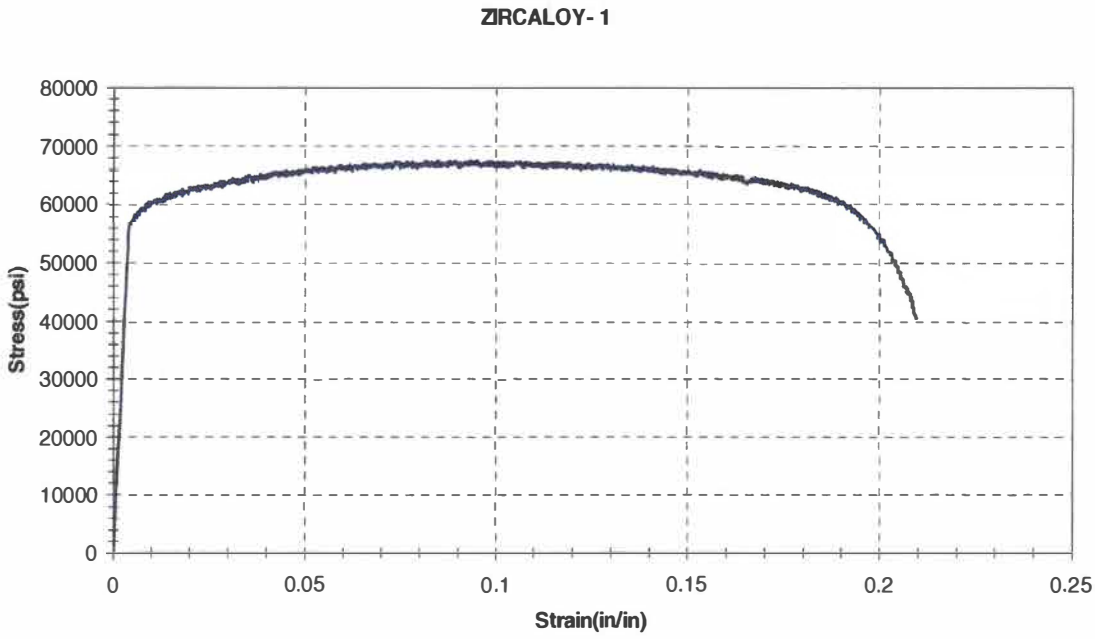

Figure 6.4: Stress-strain curve of undoped Zircaloy-4

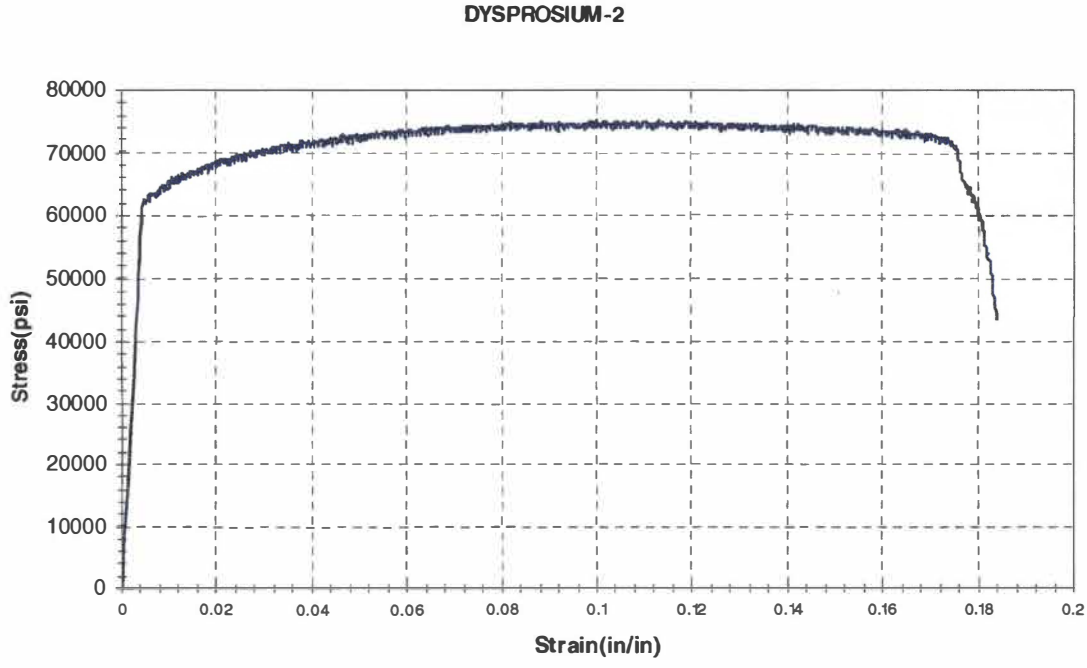

Figure 6.5: Stress-strain curve of Zircaloy-4 doped with 2% dysprosium at room temperature

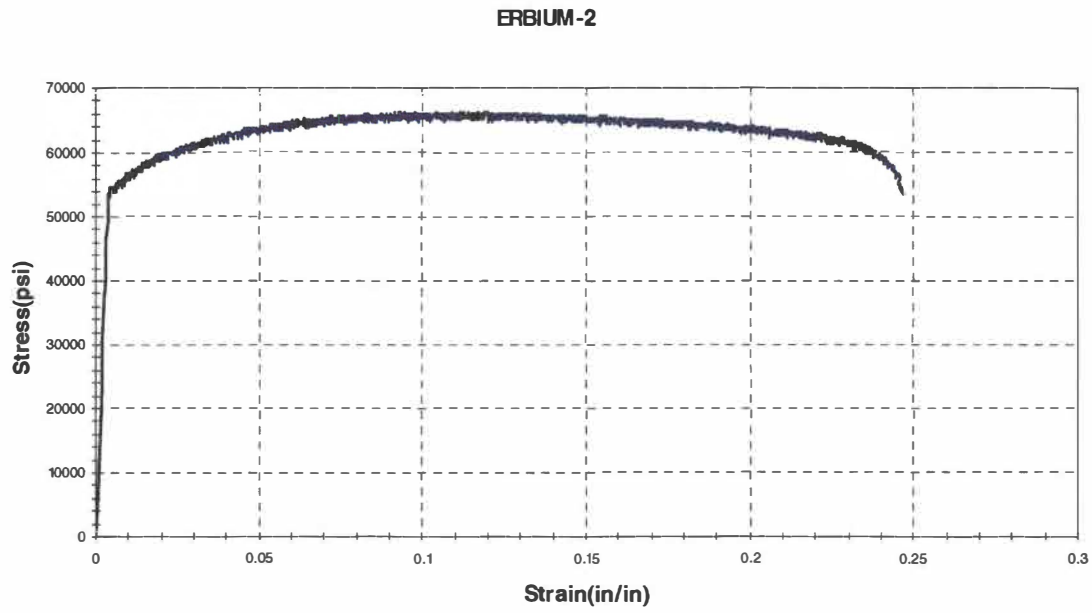

Figure 6.6: Stress-strain curve of Zircaloy-4 doped with 2% erbium at room temperature

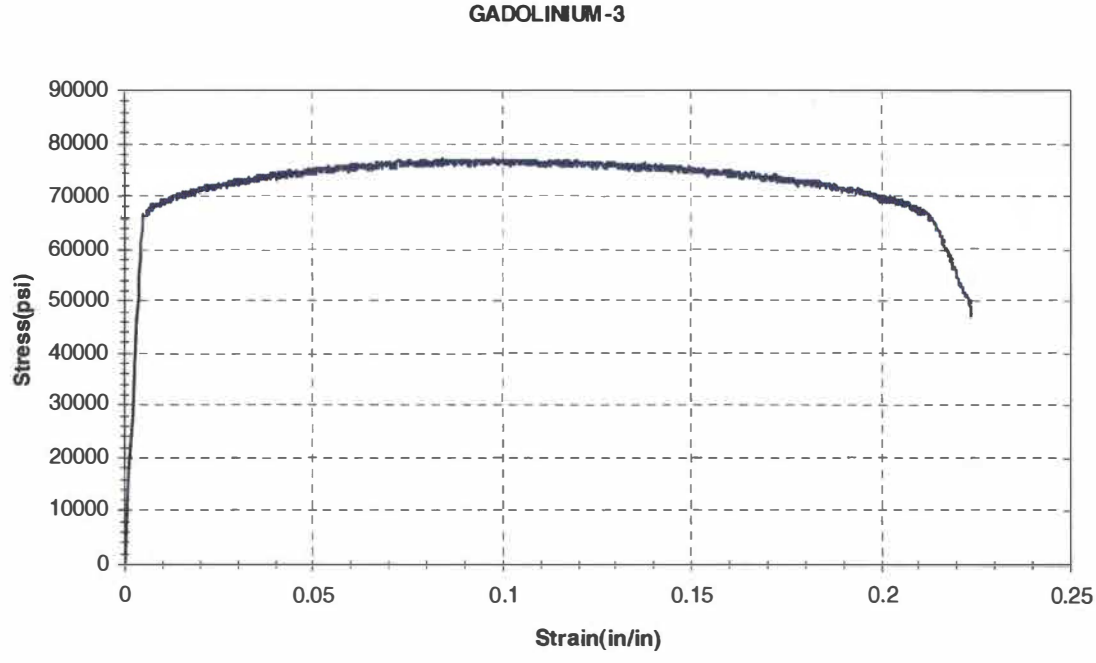

Figure 6.7: Stress-strain curve of Zircaloy-4 doped with 0.5% gadolinium at room temperature

to that of 12% for unirradiated guide tube specimens at room temperature and 9% for unirradiated cladding specimens at 300°C (572°F). Pierron, Koss and Motta have also reported 466 MPa yield strength, 488 MPa ultimate tensile strength and 10.4% elongation for mechanical properties of Zircaloy-4. It can be seen that the mechanical properties reported in the literature are higher than the experimental ones. One the other hand there is not much difference between the results reported in Table 6.1 and the vendor's data shown in Table 6.2. The difference reported is probably due to difference processes used for each material.

Table 6.2: Literature ambient-temperature mechanical properties of Zircaloy-4 alloys tested [36]

Material (Heat No.)	Vendor Certification: Wah Chang				Lab - Data: UNLV	
	YS (MPa)	UTS(MPa)	%EL	%RA	YS(MPa)	UTS(MPa)
Zircaloy-4 (243195)	379.9	548.8	23.9	58.3	384	542
Zircaloy-4 (242731)	343.3	538.4	28.5	NA	NA	NA

For information only: Vendor Test Material Certificate-Accession Numbers Mol 20030120. 1900, Mol 20030318. 0019. Data Source DID # 032HA.001

6.4.2. Fractography

Scanning electron microscopy (SEM) fractography studies were performed on the broken tensile specimens of Zircaloy-4 doped with dysprosium, erbium and gadolinium and unalloyed Zircaloy-4, used as the control material. Figure 6.8 shows the lateral side of a fractured specimen of low magnification. Besides the black spots observed on the side of the fracture end which are identified as dirt pick up prior to the tensile test, at this low magnification, only a limited-ductility fracture is apparent. Figure 6.9 reveals spherical and elongate dimples from uniaxial tensile loads. Figure 6.10 shows slip bands characteristic of plastic deformation, lending supporting evidence that doping with dysprosium did not severely embrittle the material.

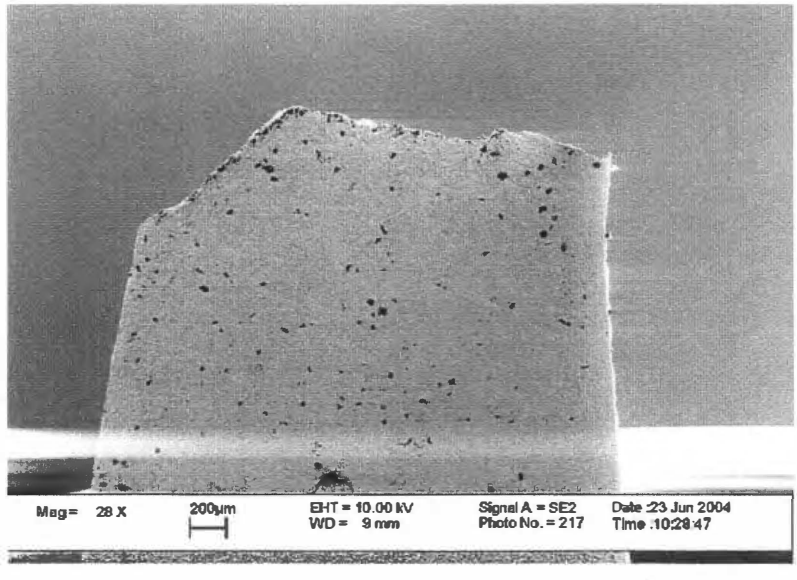

Figure 6.8: Scanning Electron Microscopy micrograph of Zircaloy-4 specimen doped with 2% dysprosium (A-Dy-1-1) at low magnification. It shows a view of the side of the fracture end which contained particles identified as dark spots

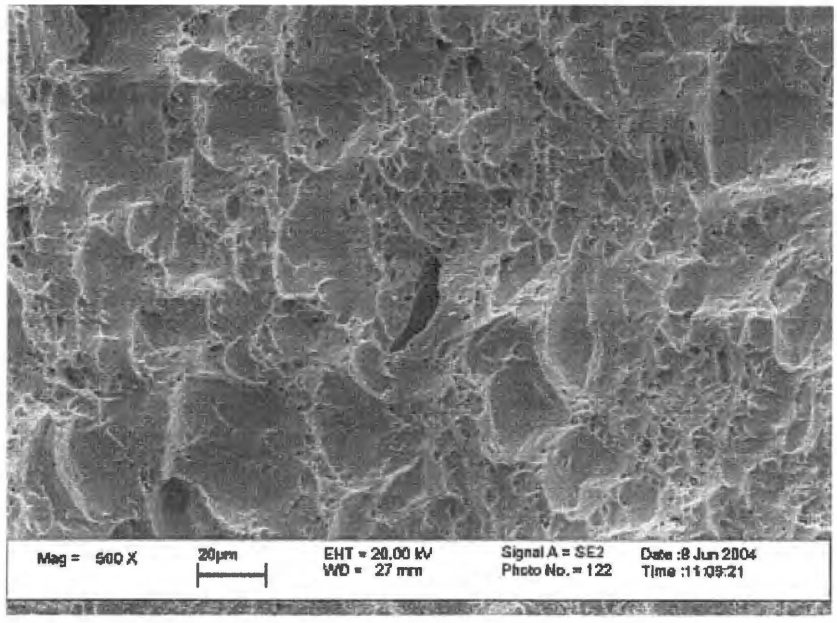

Figure 6.9: Scanning Electron Microscopy of an undoped Zircaloy-4 specimen (A-Zr-1-3) fracture surface showing spherical dimples resulting from uniaxial tensile loads and a secondary crack

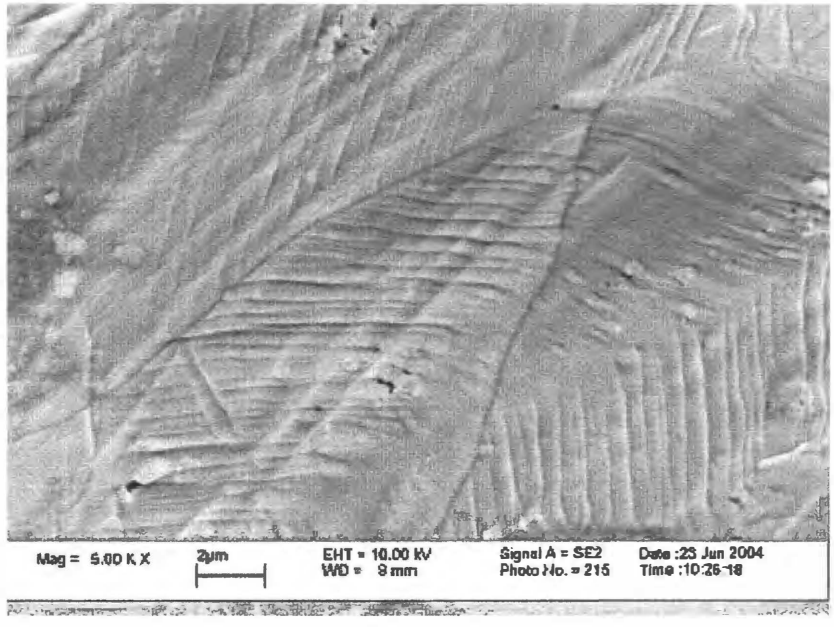

Figure 6.10: Scanning Electron Microscope micrograph of Zircaloy-4 doped with dysprosium of specimen (B-Dy-2-4) showing grain structure that contained slip lines on the surface of the fracture end.

Figure 6.15 shows the fracture surface of a Zircaloy-4 specimen doped gadolinium. Initial examination of the specimen fracture surface immediately revealed that plastic deformation is well identified even at low magnification. For more detailed studies, high magnification was used as seen from Figure 6.11, showing dimples characteristic of ductile fracture. It also exhibits dimples associated with ductile ligaments caused by microvoid coalescence that often accompanies fracture. Each dimple is one half of a microvoid that formed and then separated during the fracture process [34]. Since the ductile fracture process normally occurs in several stages, beginning with the necking process followed by microvoid formation and coalescence and continuation of crack growth, different microstructure characteristics might be formed. Shear areas characterizing a final shear fracture mode that provided more detailed information to the tensile direction were observed on Figures C-12, C-14, C-16 and C-20. Similar low and high magnification fractographs are shown for Zircaloy plus erbium in Figures 6.11 and 6.13. Again, only ductile rupture is evident on the fracture surfaces. Figures 6.14 and 6.15 show corresponding ductile features for Zircaloy-4 doped with gadolinium. Again, only ductile features are observed. EDX studies on the fracture surfaces did not reveal any concentration of rare earth elements above the doped levels. What is most significant is that intergranular fracture was never observed nor was cleavage fracture. No severe embrittlment resulting from the rare earth additions was observed.

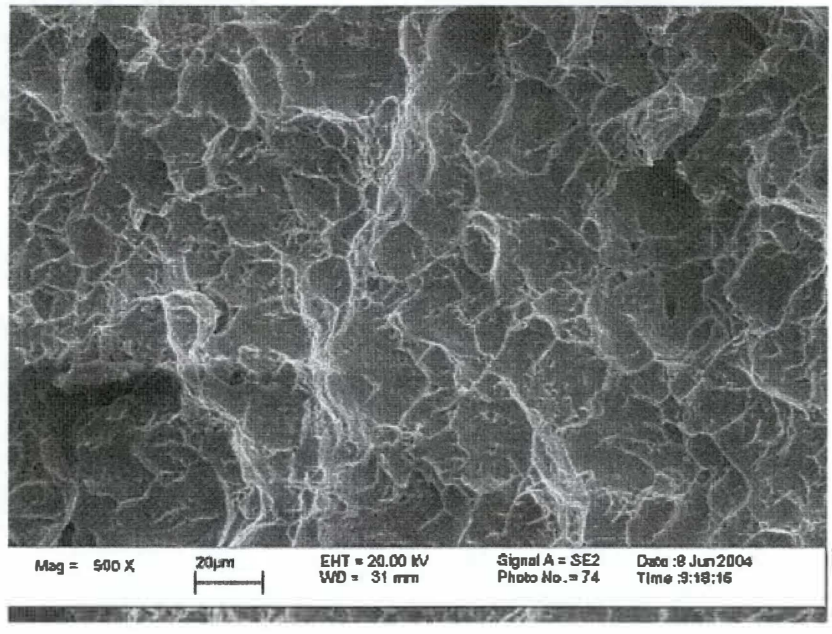

Figure 6.11: Scanning Electron Microscopy micrograph of a Zircaloy-4 specimen doped with dysprosium specimen (A-Dy-1-3) showing ductile mode fracture caused by microvoid coalescence

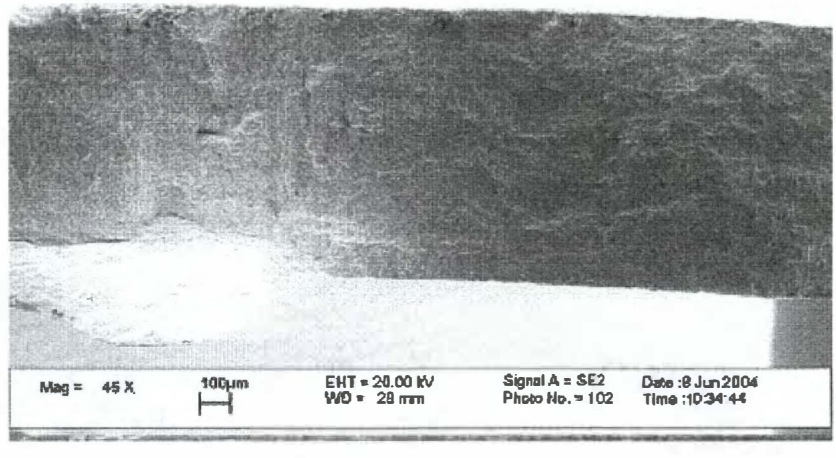

Figure 6.12: Scanning Electron Microscopy micrograph on fracture surface of Zircaloy-4 sample (A-Er-1-1) doped with 2% erbium. The fractographic examination shows plastic deformation obtained at low magnification.

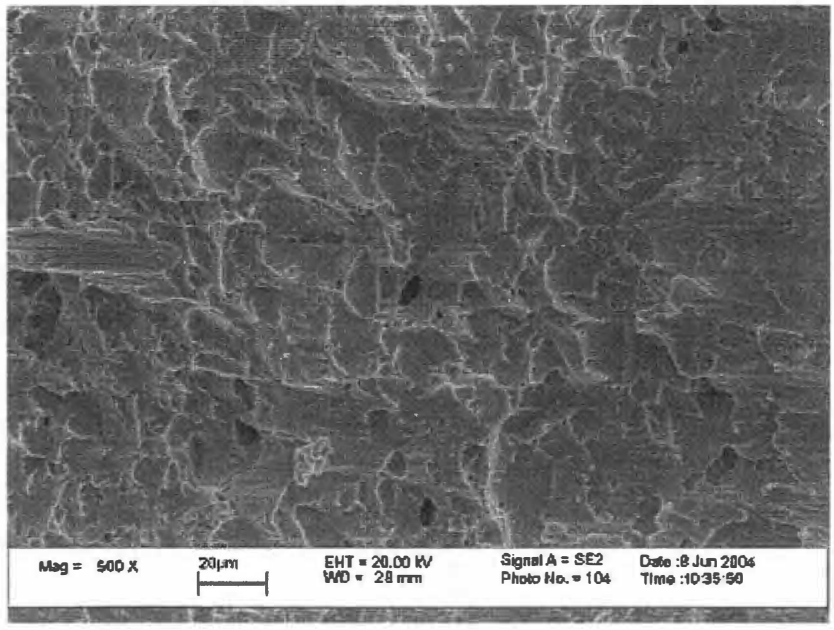

Figure 6.13: Scanning Electron Microscopy photomicrograph on fracture surface of Zircaloy-4 doped with 2% erbium specimen (A-Er-1-3) showing several microstructure features at high magnification such as dimples resulting from ductile fracture, shear and inclusions

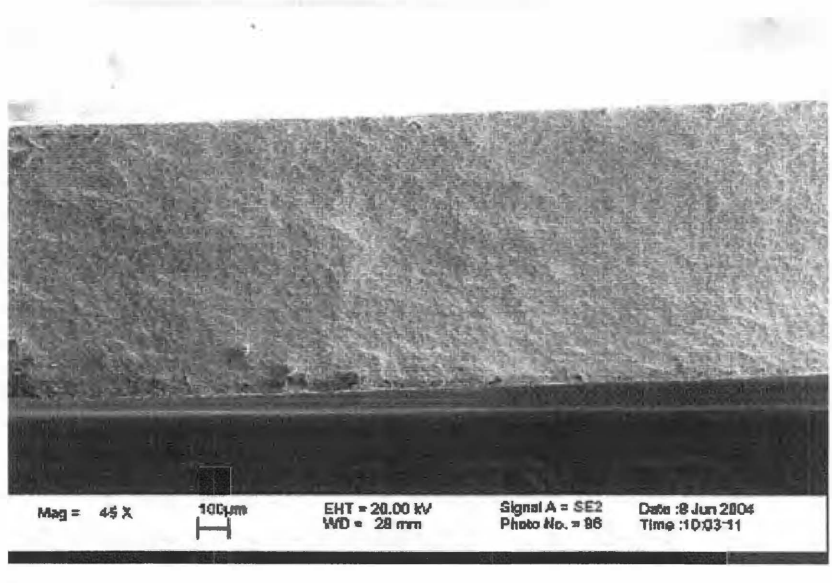

Figure 6.14: Scanning Electron Microscopy of Zircaloy-4 doped with 0.5% gadolinium specimen (B-Gd-2-1) on fracture surface showing fine-grained microstructure and plastic deformation

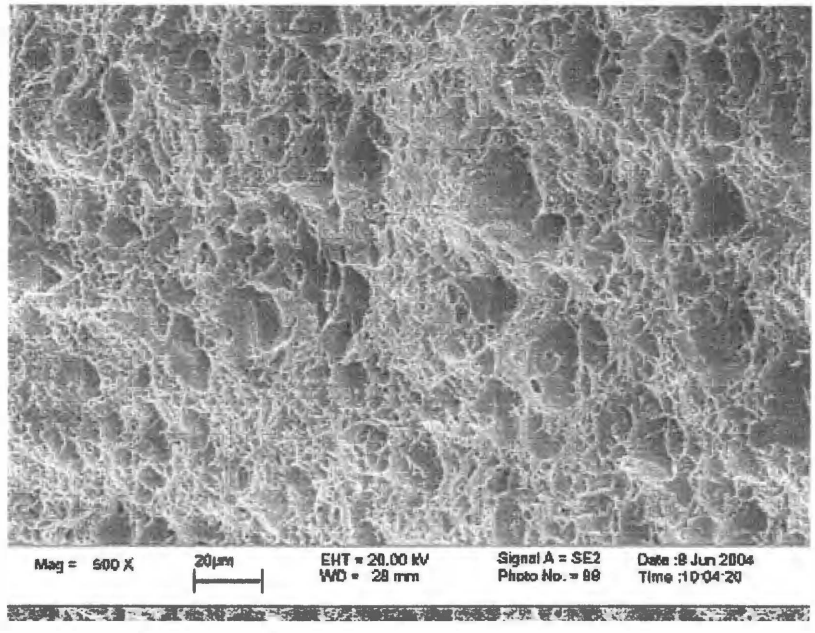

Figure 6.15: Scanning Electron photomicrograph of Zircaloy-4 doped with gadolinium of sample (B-Gd-2-3) on fracture surface showing ductile fracture with dimples associated with ductile ligaments caused by microvoid coalescence

Chapter 7

CONCLUSIONS AND FUTURE WORK

7.1. Conclusion

This thesis involves an experimental program to determine the effects of doping Zircaloy-4 with rare earth burnable poisons. Various analytical techniques have been employed in order to understand the effects of the alloying process including corrosion, scanning electron microscopy (SEM), x-ray fluorescence (EDX), optical microscopy, tensile testing and fractography. Based on the experiments and investigations conducted on Zircaloy alloys, the following specific conclusive points can be reported:

1. The tensile properties of Zircaloy-4 were not significantly affected by additions of 0.5% Gd, 2% Dy and 2% Er.
2. The corrosion resistance of Zircaloy-4 was reduced by the addition of 0.5% Gd.
3. The corrosion properties of Zircaloy-4 doped with 2% Dy or 2% Er were completely unacceptable. The failure appears to result from enhanced general attack due to addition of an active metal.
4. No segregation of any rare earth metal was observed and no intergranular embrittlment was observed. This leaves open the possibility of reducing the rare earth concentration to a safe level since it does not concentrate in local areas.

7.2 Future Work

Since this research project is the first attempt in alloying metallic rare earth elements such as dysprosium, erbium and gadolinium, serving as burnable poisons, with the fuel cladding rather than mixing with fuel in the form of compounds, there are many areas for future improvement.

The time and temperature the specimens are exposed to superheated steam in the autoclave could be crucial when corrosion occurs. Gadolinium exhibits poor corrosion and erbium and dysprosium completely transform to powder. Since detailed time and temperature data do not exist in the open literature, the characteristics of the powder should be explored to determine the effect of very high temperature and large temperature changes on the materials. Also, future experiments may be required to expose specimens in the autoclave for few hours or 10 hours maximum with intermediate neutron scattering analysis to better understand the structure of the corrosion products.

The corrosion properties of the dysprosium and erbium containing alloys were completely unacceptable. Future experiments should be conducted to determine corrosion properties of a set of alloys with varying amounts of rare earth elements to determine if it is the concentration that is critical or if it is the particular element. From the present data, it cannot be determined if it is 2% versus 0.5% concentration that is critical or if dysprosium and erbium are worse than gadolinium.

REFERENCES

REFERENCES

1. R.G. Cochran and N. Tsoulfanidis, The Nuclear Fuel Cycle: Analysis and Management American Nuclear Society, Lagrange Park, Ill., 1990, 81-87.
2. J.-P.A. Renier, M.L. Grossbeck and T. Bigelow, Development of Burnable Poisons for Commercial Nuclear Power Reactors, R011382079-01, Department of Nuclear Engineering-The University of Tennessee, 2003, 126-131.
3. L. Goldstein and A. Strasser, A Comparison of Gadolinia and Boron Poison Applications in Pressurized Water Reactors, Nuclear Technology, 60, 352, 1983
4. J.-P.A. Renier and M.L. Grossbeck, Development of Burnable Poisons for Commercial Nuclear Power Reactors, ORNL-TM-2001/238, Oak Ridge National Laboratory, 2001, 1-7.
5. A. Jonsson et al., Analysis of Critical Experiments with Erbia – Uranium Fuel, Trans. Am. Nucl. Soc., 65 and 415, 1992.
6. P.M. O'Leary and M.L. Pitts, Effects of Burnable Absorbers on PW Spent Nuclear Fuel, WM'01 Conference, Tucson, 2001.
7. J.C. Wagner and C.V. Parks, Parametric Study of the Effect of Burnable Poison Rods for PWR Burnup Credit, ORNL-TM-2000373, Oak Rigde National Laboratory, 2002, 1-3.
8. L. SungJoon, P. ChanJin, L. YunSoo and K. HyukSang, Influences of laser surface alloying with niobium (Nb) on the corrosion resultance of Zircaloy-4, Journal of Nuclear Materials 321, 177-183, 2003
9. S. Farina, G. Duffo and J. Galvele, Stress Corrosion of Zircaloy-4 in Halide Solutions. Effect of Temperature, Materials Research, Vol. 5, No. 2, 107-112, 2002
10. S. Narayane, B. Rao and B. Kashyap, Development and validation of a processing for zirconium alloys, Modelling Simul. Mater. Sci. Eng. 10, 503-520, 2002
11. J. Schemel, ASTM Manual on Zirconium and Hafnium, American Society of Testing and Materials, 1-88, 1977
12. S. Glasstone, Principles of Nuclear Reactor Engineering, D. Van Norstrand Company, Inc., Princeton, New Jersey, 507-513 and 765-767, 1955.

13. M. Speer, LWR Fuel Pin Performance during Burnup, Department of Nuclear Engineering University of California, Berckely

14. W. Cahn, P. Haasen, J. Kramer, D. Frost and T. Brian, Materials Science and Technology, A Comprehensive Treatment, Volume 10A, Nuclear Materials, Part I, VCH Publishers Inc., New York, 114-179, 1994.

15. W. K. Anderson Ed., Corrosion of Zirconium Alloys, ASTM STP 368, Philadelphia, 3-22, 1964

16. K. Une and S. Ishimoto, Dissolution and precipitation behavior of hydrides in Zircaloy-2 and high Fe Zircaloy, Journal of Nuclear Materials 322, 66-72, 2003

17. C. Forty and P. Karditsas, Uses of zirconium alloys in fusion applications, Journal of Nuclear Materials 283-287, 607-610, 2000.

18. H. Hong, S. Kim and K. Lee, Influence of dilute silicon addition on the oxidation resistance and tensile properties of modified Zircaloy-4, Journal of Nuclear Materials 304, 8-14, 2002.

19. G. Bertolino, G. Meyer and J. Ipina, Effects of hydrogen content and temperature on fracture toughness of Zircaloy-4, Journal of Nuclear Materials 320, 272-279, 2003.

20. M. Oskarsson, E. Ahlberg and K. Pettersson, Oxidation of Zircaloy-2 and Zircaloy-4 in water and lithiated water at 360°C, journal of Nuclear Materials 295, 97-108, 2001

21. C. R. Tipton, Jr., Reactor Handbook Second Edition, Volume I Materials, 709-734, 1960

22. A. Buch, Pure Metals Properties: A Scientific-Technical Handbook, ASM International, 19, 1999

23. B. Hindin, Report on Testing Zirconium Alloys according to ASTM G 2 for 336 hours in steam at 750 F, Battelle, 1-7, 2003.

24. Applications-Related Phenomena in Zirconium and its Alloys, ASTM special technical publication 458, 360-371,1969

25. Standard Test Method for Corrosion Testing of Products of Zirconium, Hafnium, and Their Alloys in Water at 680°F or in Steam at 750°F, Designation: G 2-88 (Reapproved 1996), 1- 4.

26. J. B. Bindell, Scanning Electron Microscopy

27. G.F.V. Voort, Metallography Principles and Pratice, McGraw-Hill ASM International, New York, c1984

28. H. Hong, S. Kim and K. Lee, Influence of dilute silicon addition on the oxidation resistance and tensile properties of modified Zircaloy-4, Journal of Nuclear Materials 304, 8-14, 2002.

29. J. Goldstein, D. Newbury, P. Echlin, D. Joy, A. Romig, C. Lyman, C. Fiori and E. Lifshin, Scanning Electron Microscopy and X-Ray Microanalysis, Second Edition, Plenum Press, New York and London, 1992,

30. R. J. Parrington, Tutorial: Fractography of Metals and Plastics, Volume 2(5), 2002

31. W. D. Callister, Jr., Materials Science and Engineering: An Introduction, Department of Metallurgical Engineering, The University of Utah, John Wiley & Sons, Inc., Danvers, MA, 112-194,2003

32. G. Bertolino, G. Meyer and J. P. Ipina, Degradation of the mechanical properties of zircaloy-4 due to hydrogen embrittlement, Journal of Alloys and Compounds 330-332 (2002) 480-413

33. D.Q. Peng, X.D. Bai, X.W. Chen, Q.G. Zhou, X.Y. Liu and R.H. Yu, Comparison of electrochemical behavior of zirconium and zircaloy-4 implanted with Y and Ce ions, Applied Surface Science, Beijing, 260-271, 2003

34. Standard Test Method for Determination Average Grain Size

35. S. K. Yagnik, Y. R. Rashid and R.L. Yang, Effect of Hydrides on the Mechanical Properties of Zircaloy-4, International Meeting on LWR Fuel Performance, 2004

36. A. Roy, Task 32 Delayed Hydride Cracking of Spent Fuel Cladding under Repository Conditions, University of Community college system of Nevada, TR-03-010, 2003 (for Table 6.2)

APPENDIXES

Appendix A

ADDITIONAL TENSILE TEST RESULTS

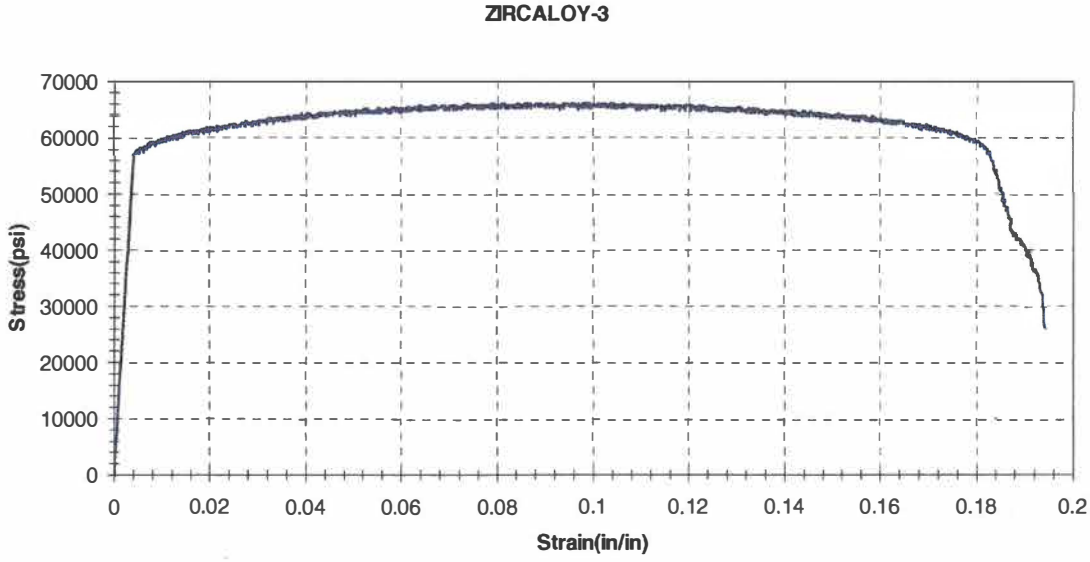

Figure A.1: Stress – strain curve of undoped Zircaloy-4-3 specimen at room temperature

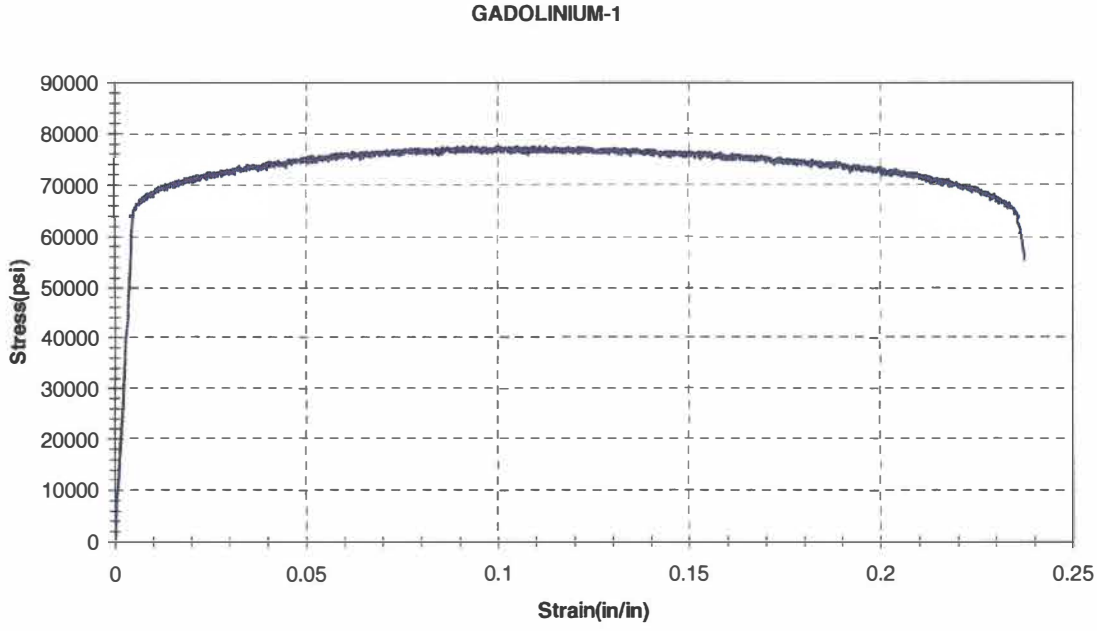

Figure A.2: Stress – strain curve of Zircaloy-4 specimen doped with 0.5% gadolinium-1 at room temperature

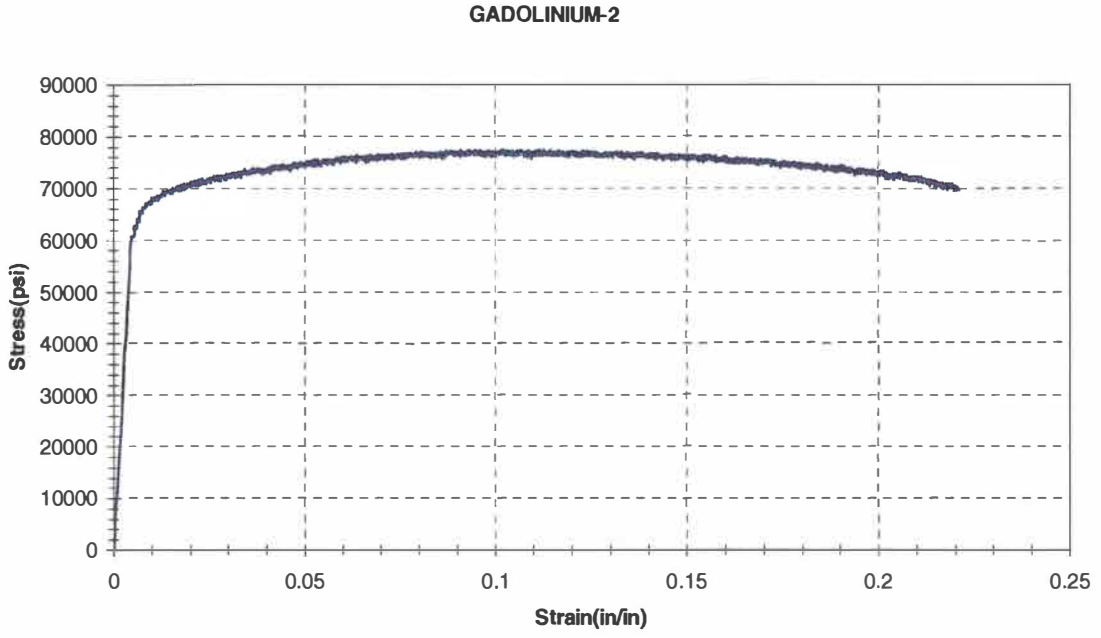

Figure A.3: Stress – strain curve of Zircaloy-4 specimen doped with 0.5% gadolinium-2 at room temperature

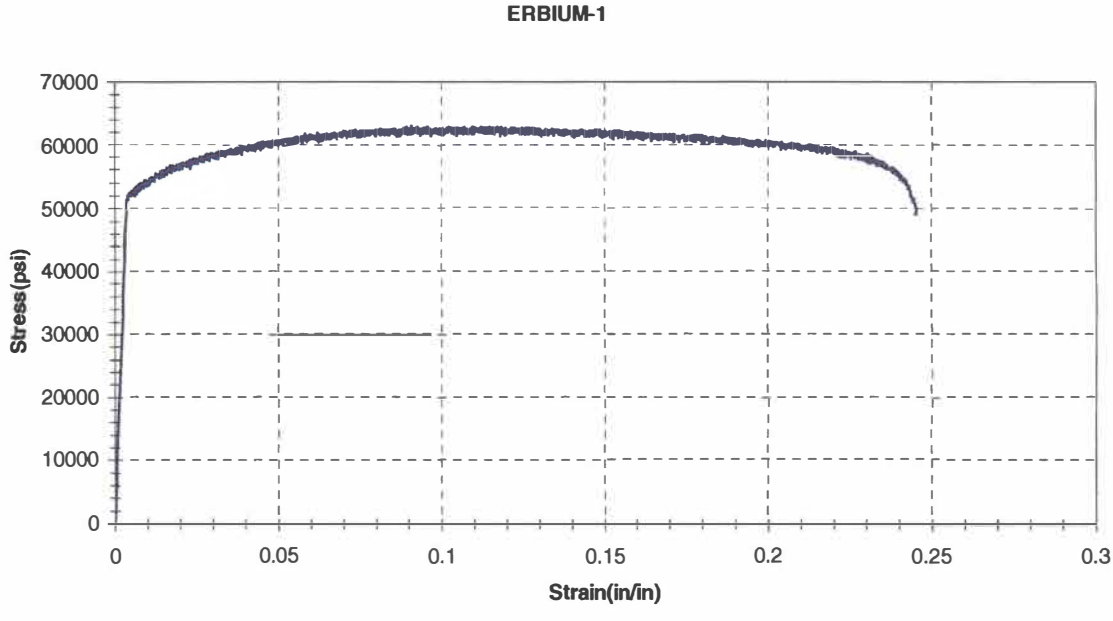

Figure A.4: Stress-strain curve of Zircaloy-4 specimen doped with 2% erbium-1 at room temperature

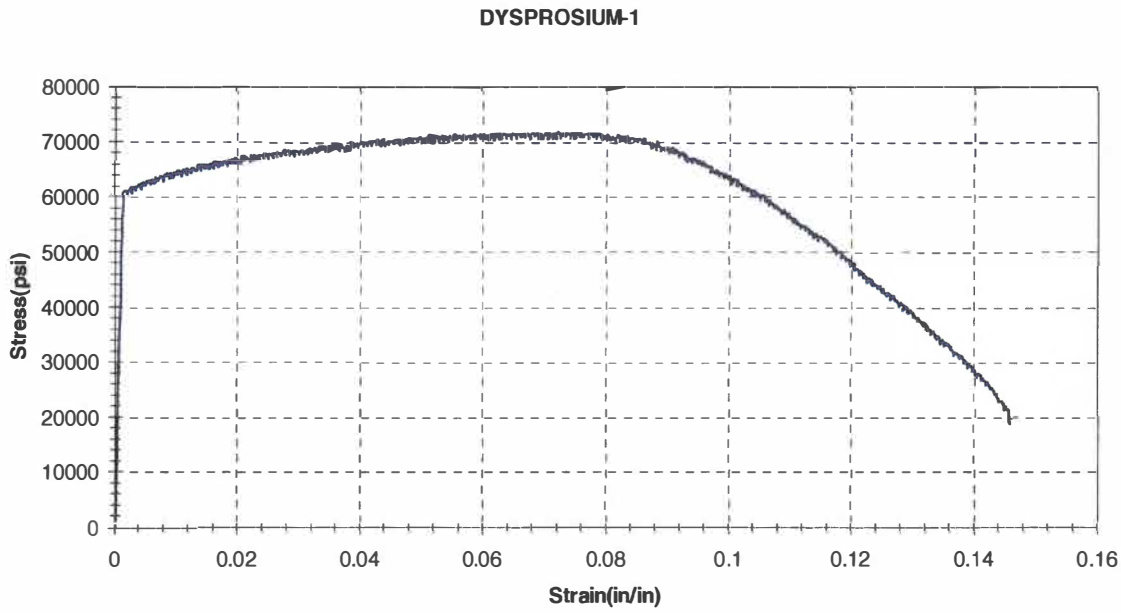

Figure A.5: Stress-strain curve of Zircaloy-4 specimen doped with 2% dysprosium-1 at room temperature

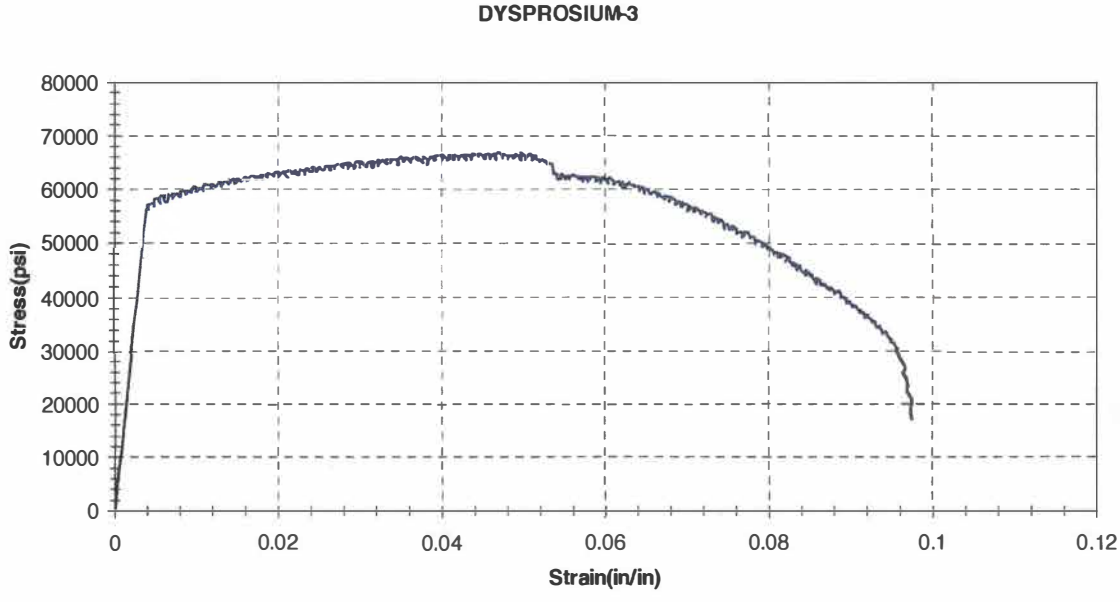

Figure A.6: Stress-strain curve of Zircaloy-4 specimen doped with 2% dysprosium-3 at room temperature.

Appendix B

TENSILE TEST CURVES AS OUPUT DIRECTLY FROM THE TENSILE MACHINE

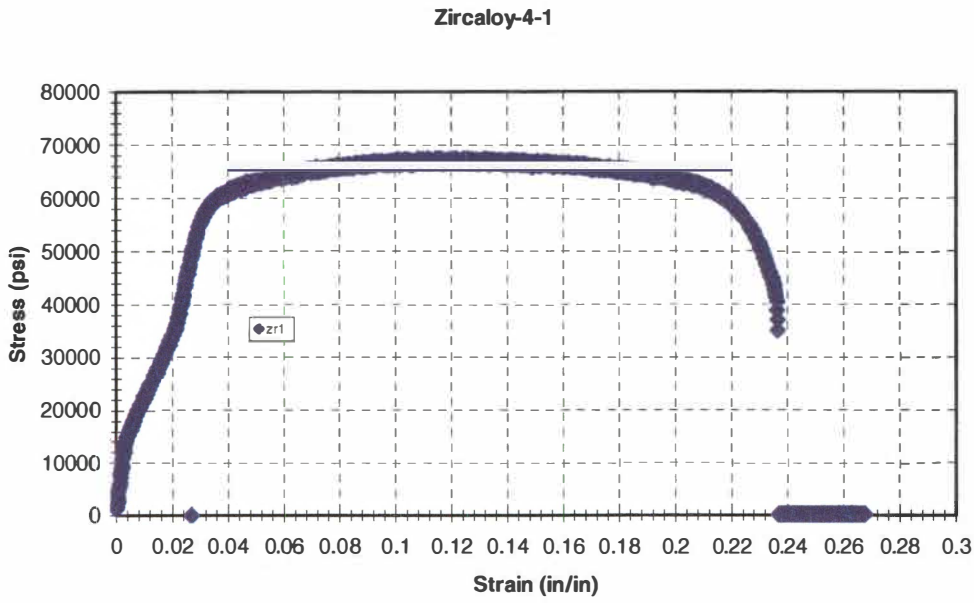

Figure B-1: Stress – strain behavior of free Zircaloy-4

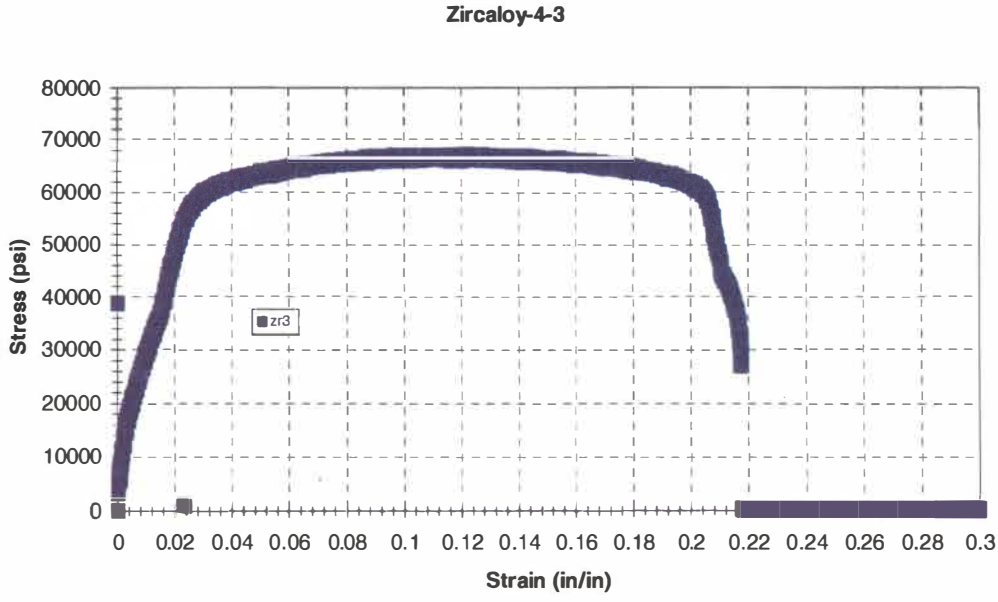

Figure B-2: Stress – strain behavior of free Zircaloy-4 specimen-3

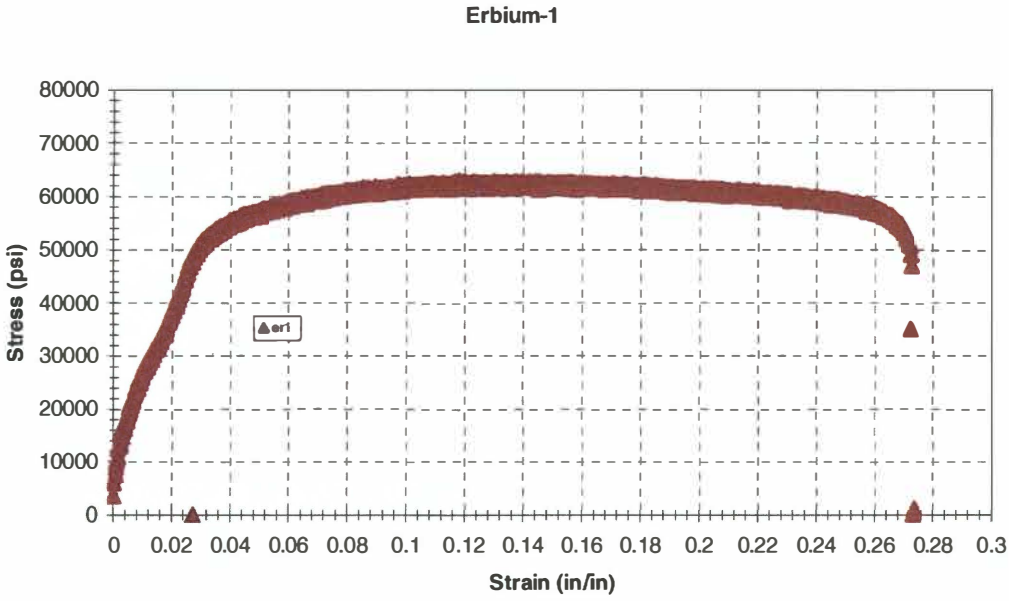

Figure B-3: Stress-strain behavior of Zircaloy-4 specimen-1 doped with 2% erbium

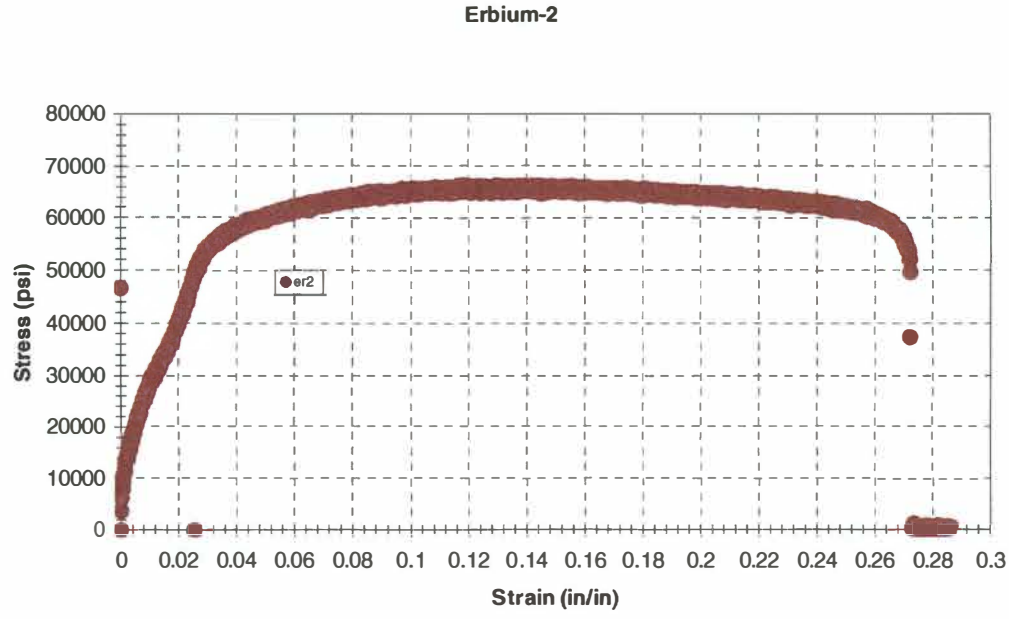

Figure B-4: Stress-strain behavior of Zircaloy-4 sprcimen-2 doped with 2% erbium

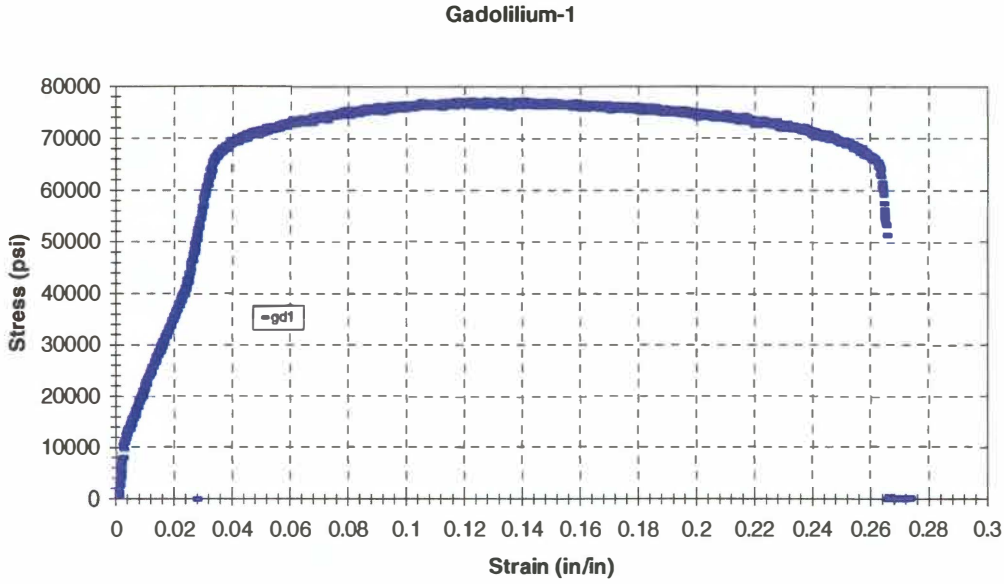

Figure B-5: Stress –strain behavior of Zircaloy-4 specimen-1 doped with 0.5% gadolinium

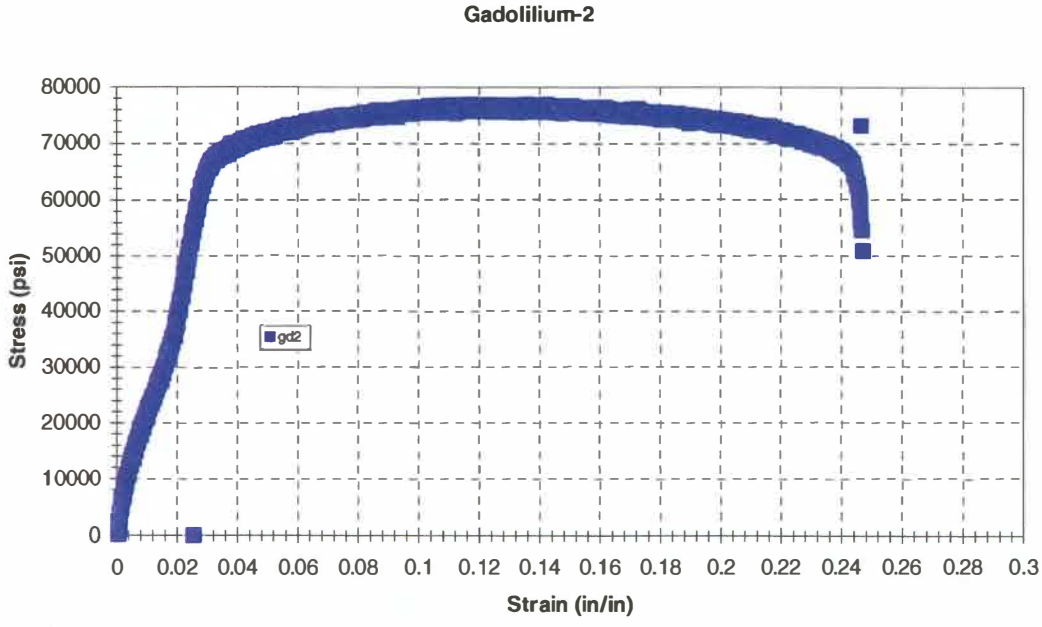

Figure B-6: Stress-strain behavior of Zircaloy-4 specimen-2 doped with 0.5% gadolinium

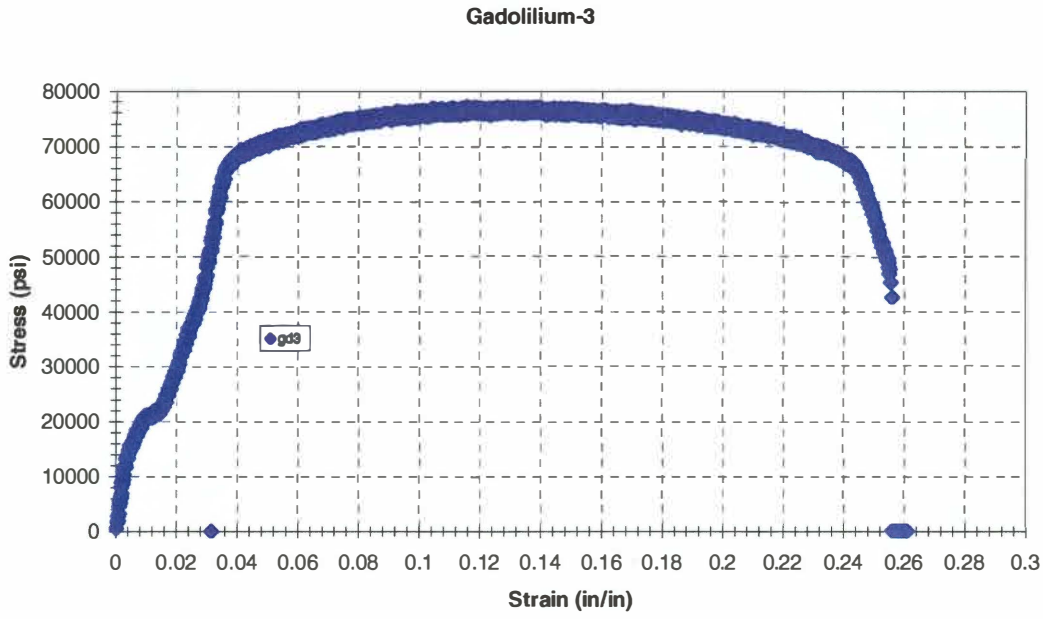

Figure B-7: Stress –strain behavior of Zircaloy-4 specimen-3 doped with 0.5% gadolinium

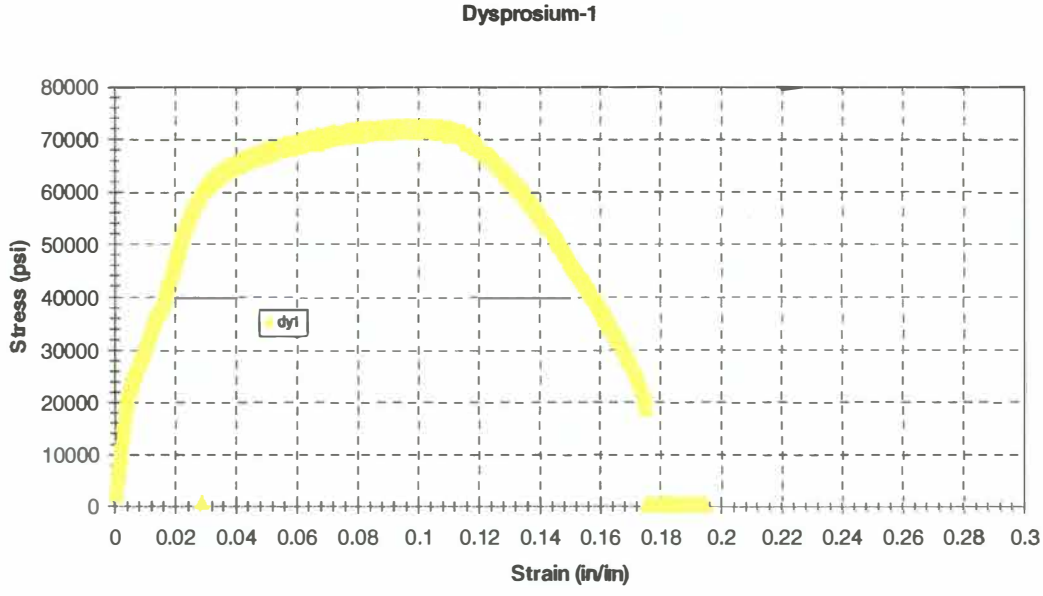

Figure B-8: Stress – strain behavior of Zircaloy-4 specimen-1 doped with 2% dysprosium

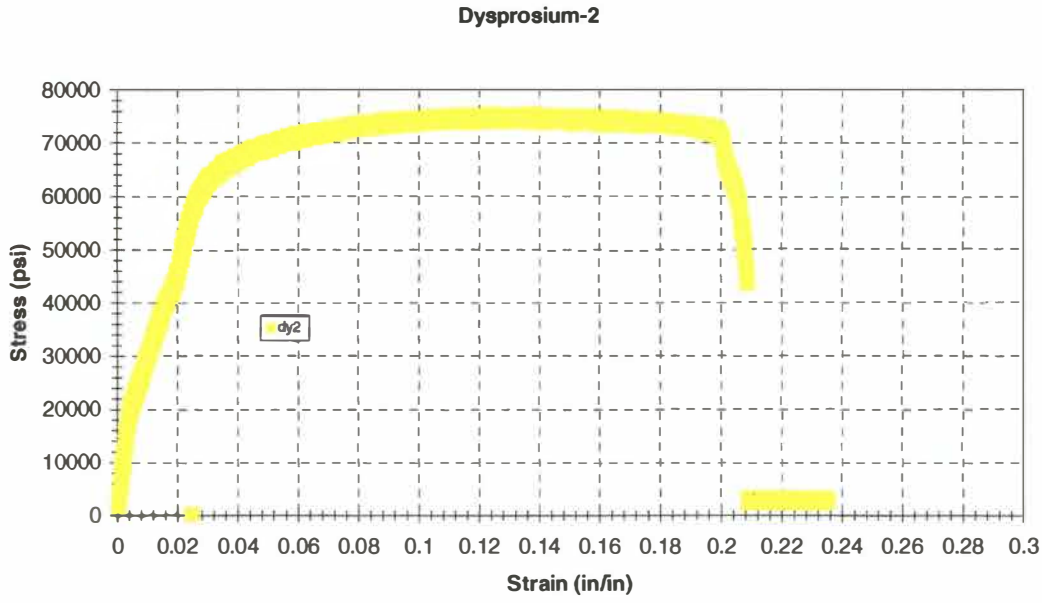

Figure B-9: Stress –strain behavior of Zircaloy-4 specimen-2 doped with 2% dysprosium

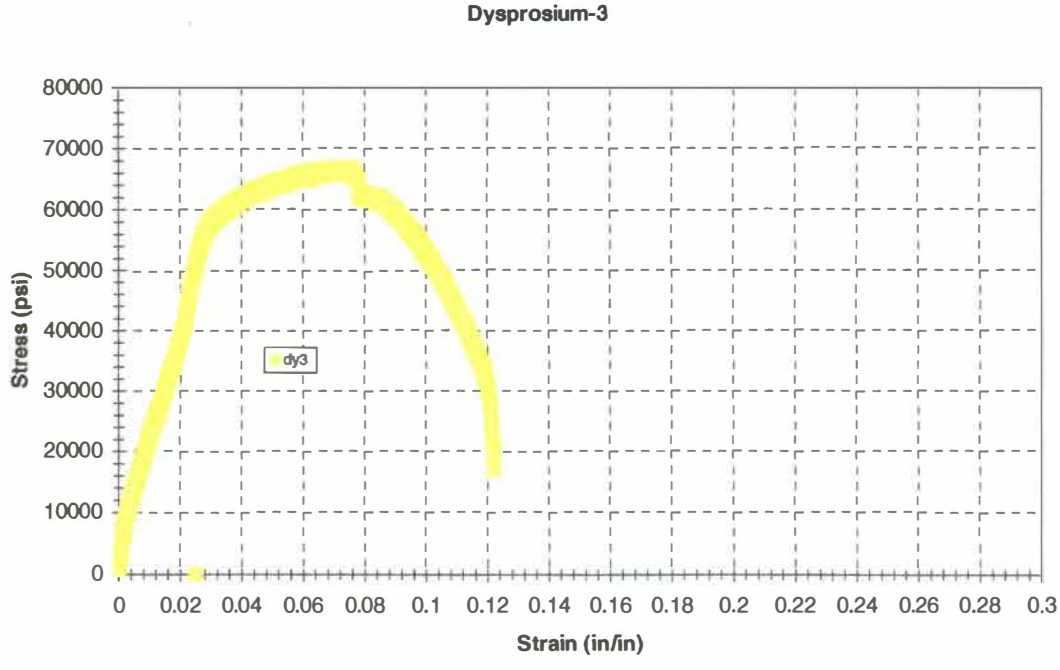

Figure B-10: Stress - strain behavior of Zircaloy-4 specimen-3 doped with 2% dysprosium

Appendix C

FRACTOGRAPHY

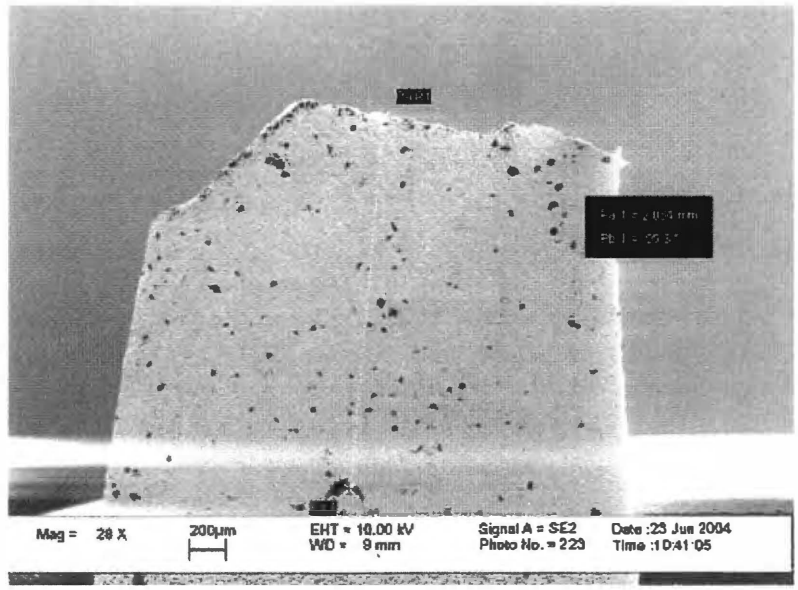

Figure C-1: Scanning Electron Microscopy micrograph of Zircaloy-4 specimen doped with 2% dysprosium (A-Dy-1-7) developed at low magnification. It can be seen that a large crack was localized on the fracture end.

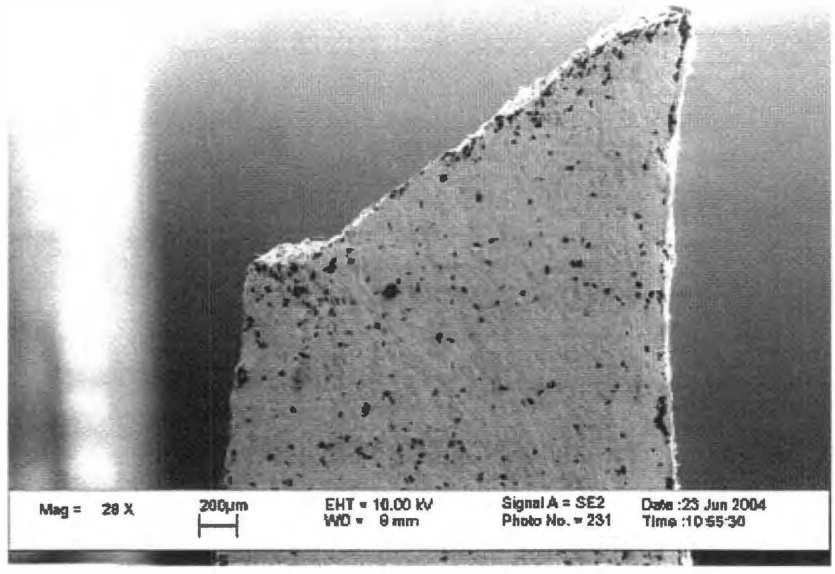

Figure C-2: The fractography micrograph of undoped Zircaloy-4 (A-Zr-1-1) specimen developed at low magnification, showing a view of the side of the fracture end which contained dirt particles identified as dark spots

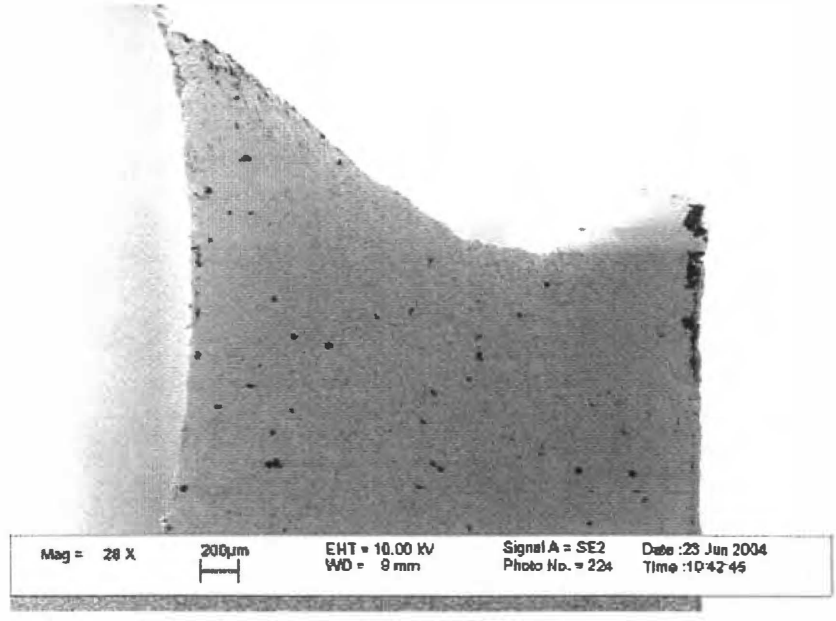

Figure C-3: Scanning Electron Microscopy micrograph of Zircaloy-4 doped with 2 percent dysprosium of specimen (C-Dy-3-1) at low magnification

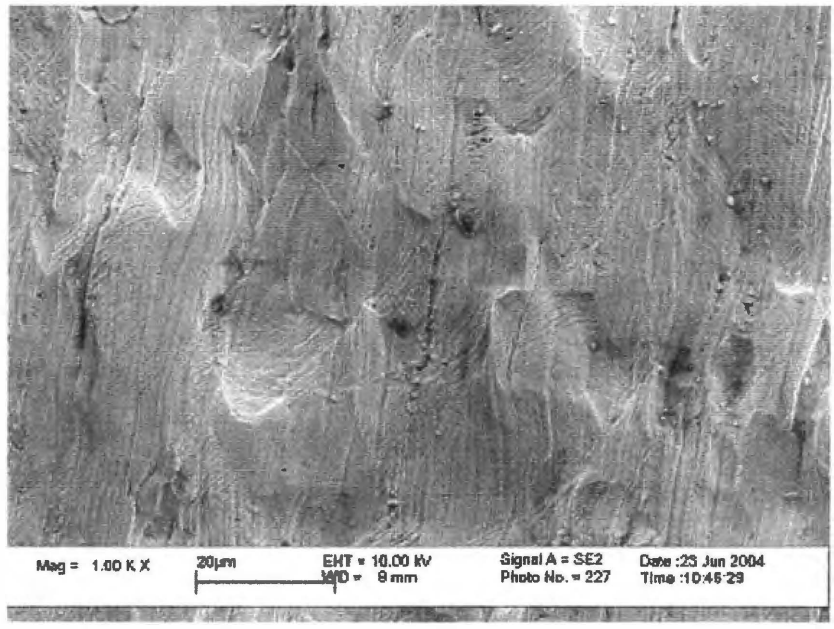

Figure C-4: Scanning Electron Microscopy micrograph of Zircaloy-4 doped with 0.5 percent dysprosium of specimen (C-Dy-3-4) on the surface of the fracture end at high magnification

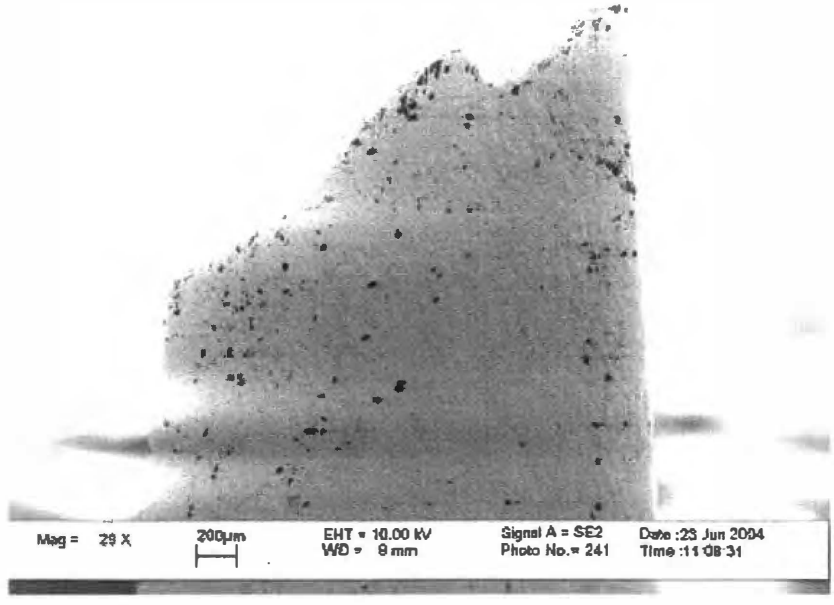

Figure C-5: Scanning Electron Microscopy micrograph of undoped Zircaloy-4 of specimen (C-Zr-3-1)

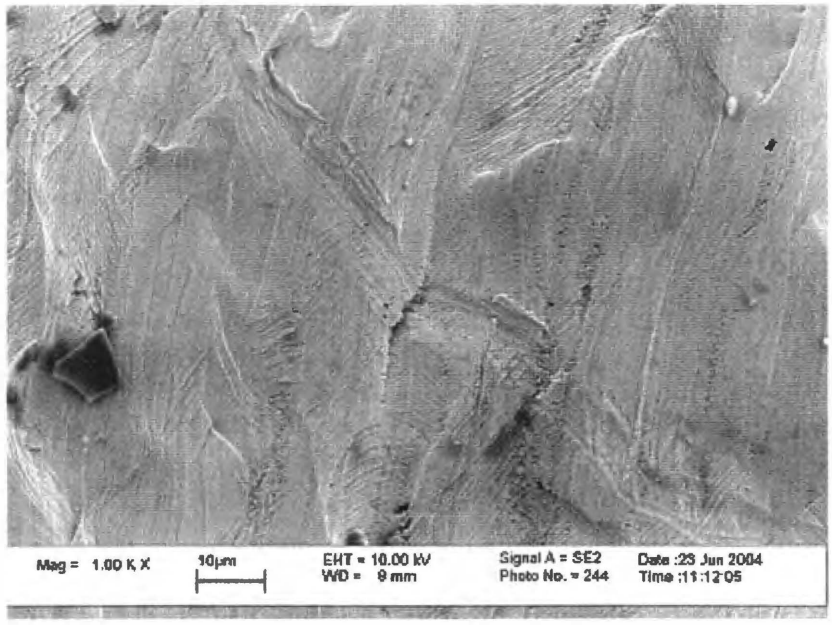

Figure C-6: Scanning Electron Microscopy of free Zircaloy-4 of specimen (C-Zr-3-4). It reveals slip lines, rough surfaces and dirt particles at high magnification

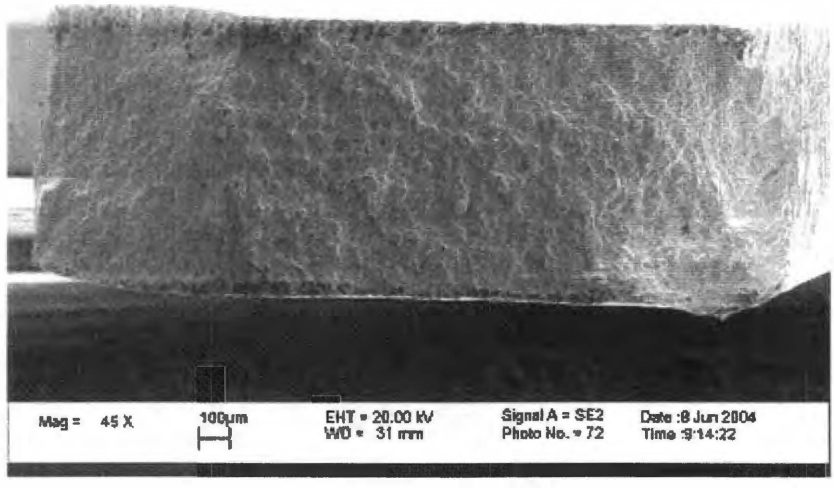

Figure C-7: Scanning Electron Microscopy of Zircaloy-4 doped with 2 percent dysprosium of specimen (A-Dy-1-1) showing plastic deformation that is a fundamental measurement of ductility.

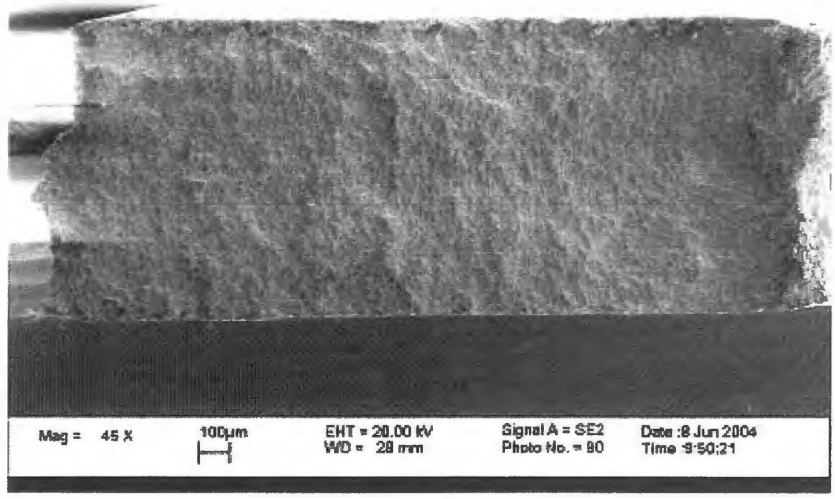

Figure C-8: Scanning Electron Microscopy of Zircaloy-4-Gadolinium specimen (A-Gd-1-1) on fracture surface showing plastic deformation

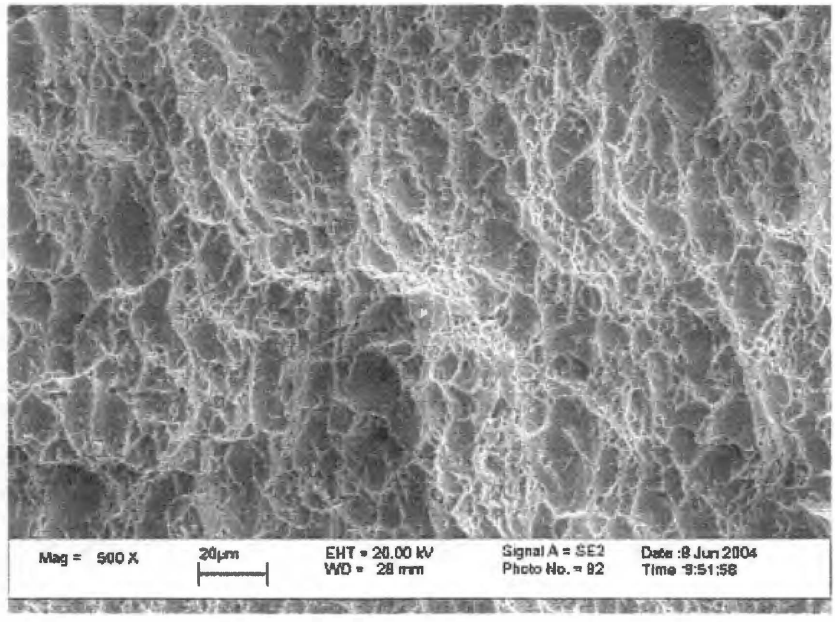

Figure C-9: Scanning Electron Microscopy of Zircaloy-4-Gadolinium specimen (A-Gd-1-3) on fracture showing dimples caused by microvoid coalescence.

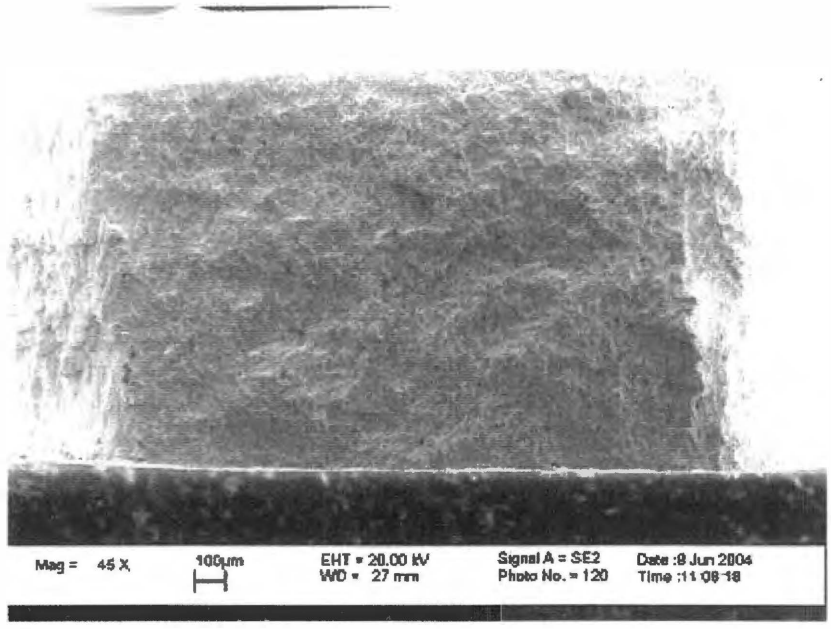

Figure C-10: Scanning electron photomicrograph of undoped Zircaloy-4 specimen (A-Zr-1-1) on fracture surface exhibiting plastic deformation

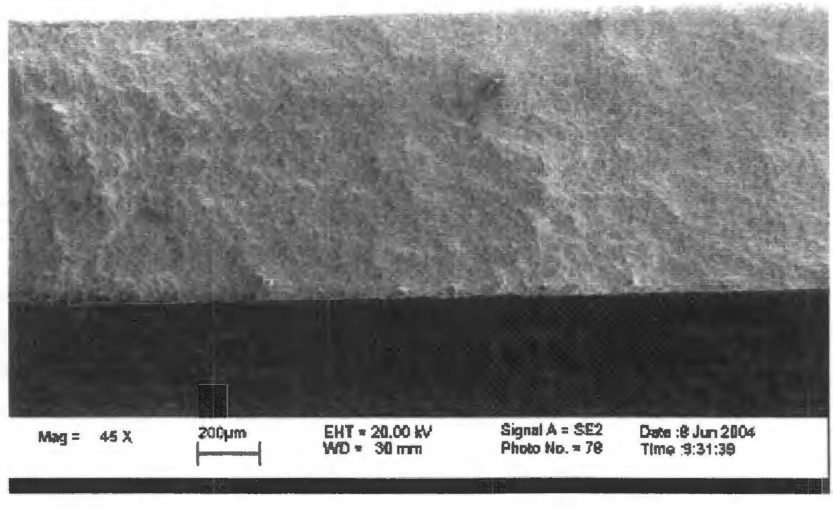

Figure C-11: Scanning Electron Microscopy of Zircaloy-4-Dysprosium specimen (B-Dy-2-1) on fracture surface showing plastic deformation

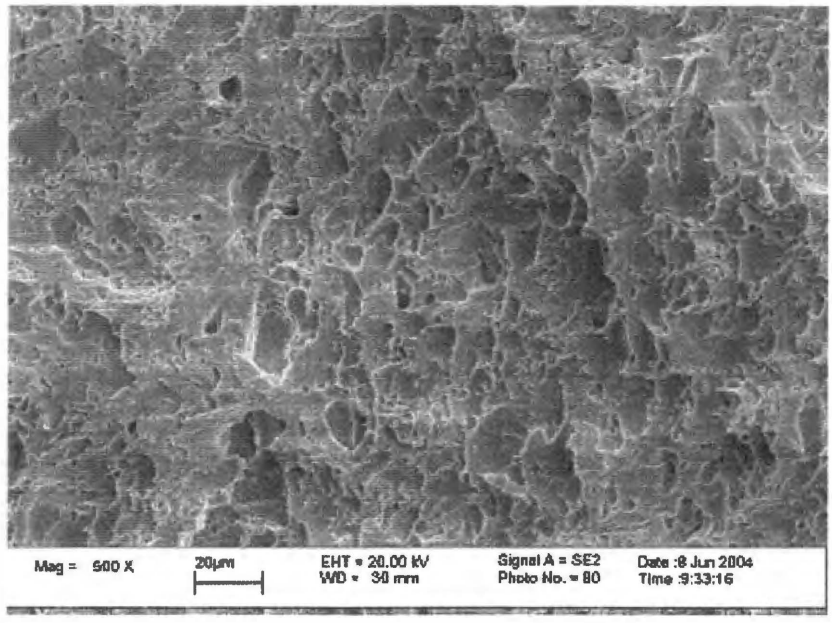

Figure C-12: Scanning Electron Microscopy of Zircaloy-4 doped with 2 percent dysprosium of specimen (B-Dy-2-3) on fracture surface revealing a transition of shear deformation and elongate dimples

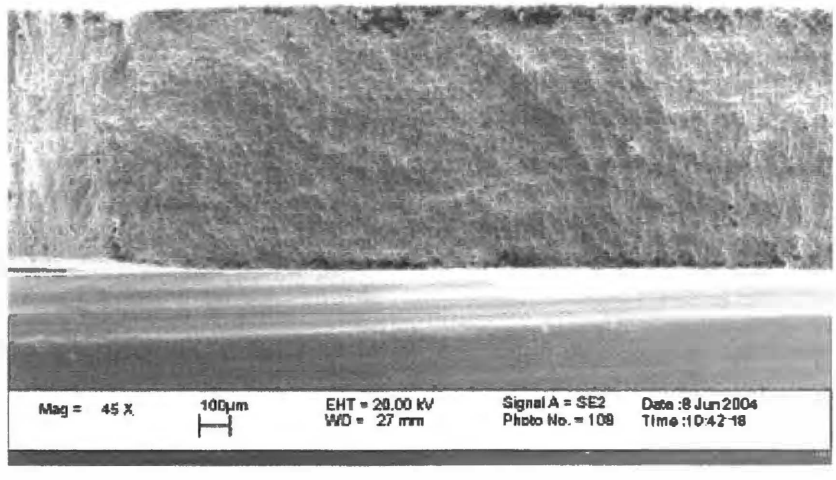

Figure C-13: Scanning Electron Microscopy of Zircaloy-4 doped with 2 percent erbium of specimen (B-Er-2-1) on fracture surface presenting plastic deformation at low magnification

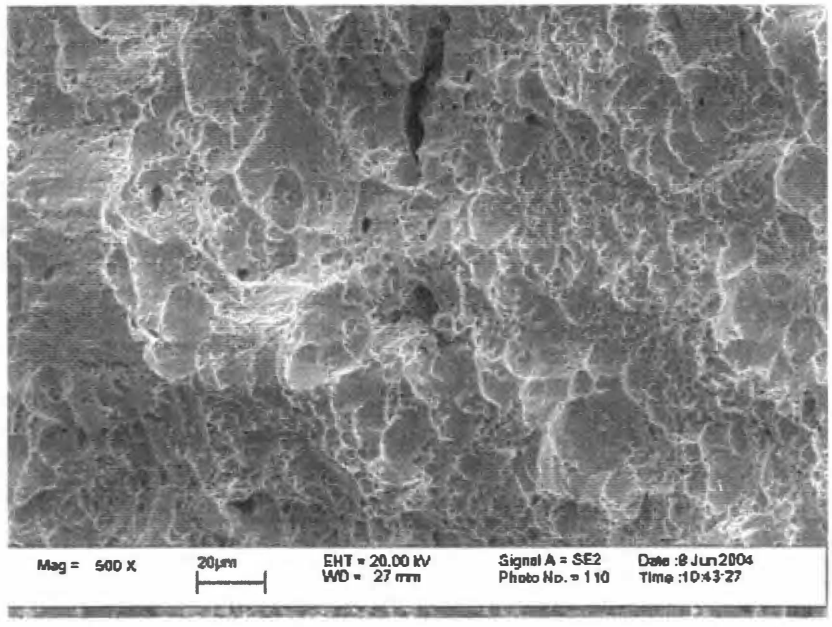

Figure C-14: Scanning Electron Microscopy of Zircaloy-4 doped with erbium of specimen (B-Er-2-3) showing typical ductile fracture surface that contained large crack. No segregation could be detected on the secondary crack surfaces. The crack is rare event possibly initiated by an inclusion

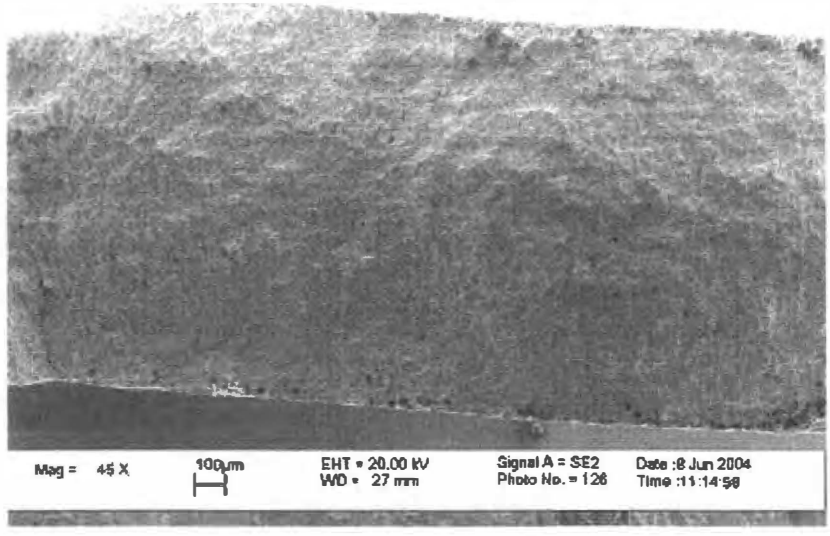

Figure C-15: Scanning Electron Micrograph of free Zircaloy-4 specimen (B-Zr-2-1) on fracture surface showing plastic deformation

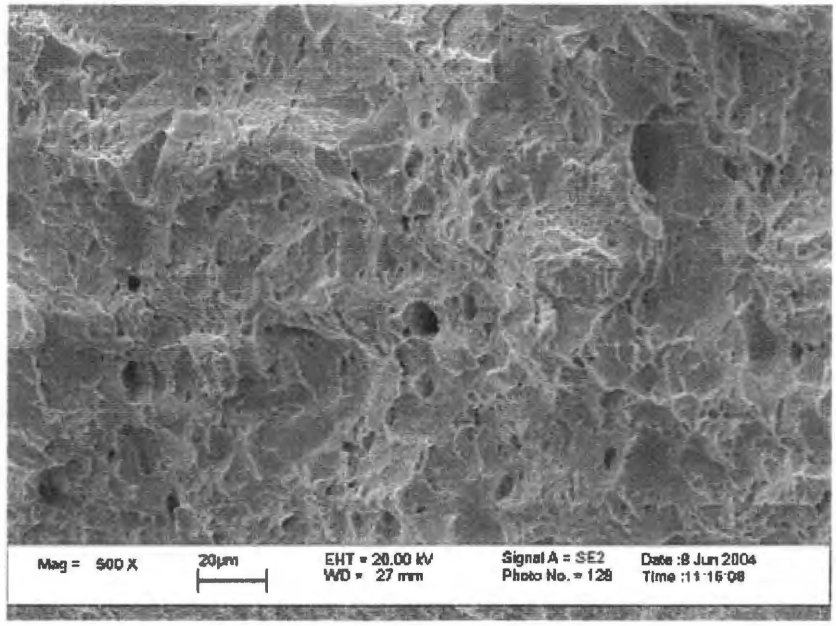

Figure C-16: Scanning Electron Micrograph of undoped Zircaloy-4 of specimen (B-Zr-2-3) showing fracture surface that reveals shear and plastic deformation

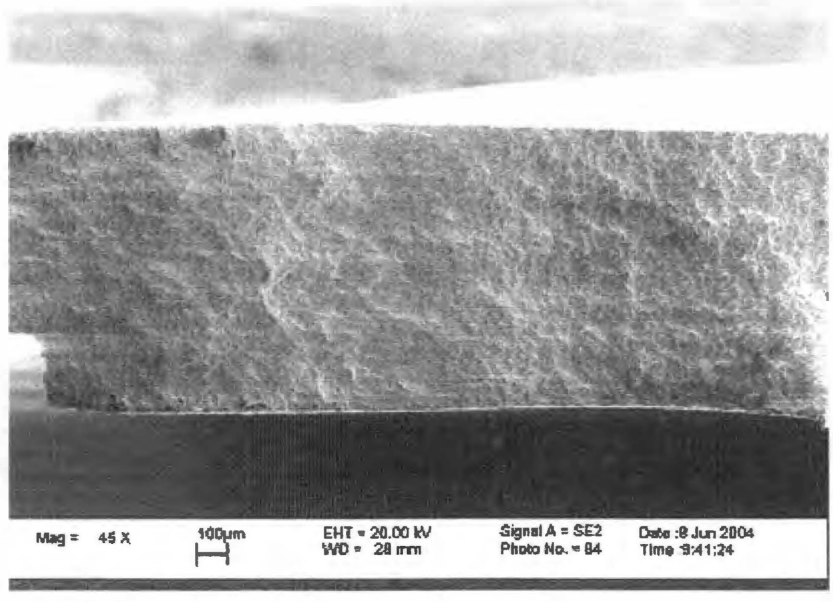

Figure C-17: Scanning Electron Microscopy of Zircaloy-4 doped with 2 percent dysprosium of specimen (C-Dy-3-1) on fracture surface revealing plastic deformation

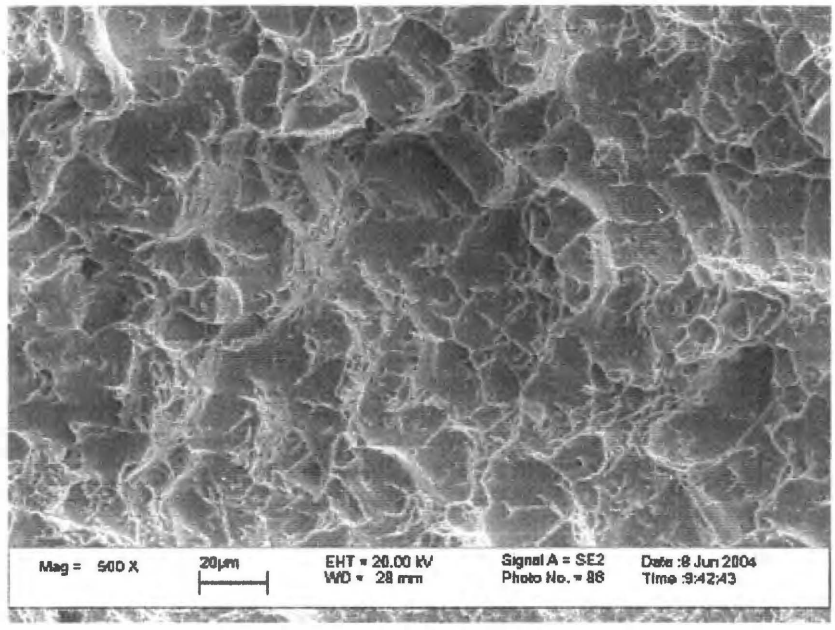

Figure C-18: Scanning Electron Microscopy of Zircaloy-4 doped with dysprosium of specimen (C-Dy-3-3) on fracture surface showing spherical dimples characteristic of ductile fracture resulting from initial tensile loads.

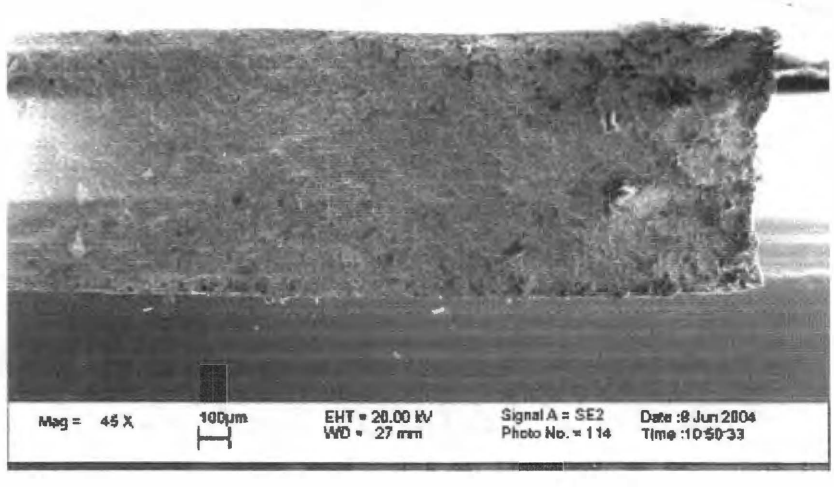

Figure C-19: Scanning Electron Microscopy of Zircaloy-4 doped with 2 percent erbium of specimen (C-Er-3-1) on fracture surface showing plastic deformation associates with few particles of dirt

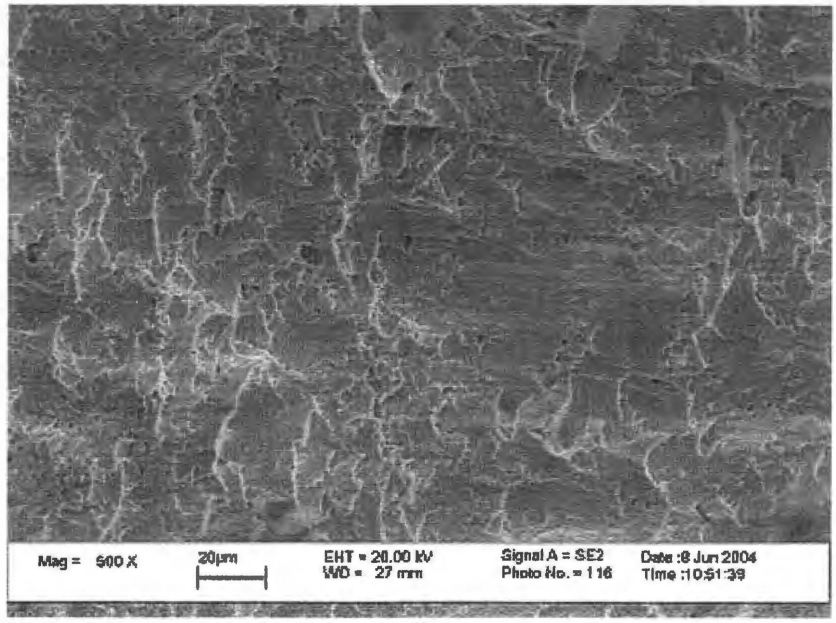

Figure C-20: Scanning Electron Microscopy of Zircaloy-4 doped with 2 percent erbium of specimen (C-Er-3-3) on fracture surface showing shear deformation and few dimples caused by fracture ductile

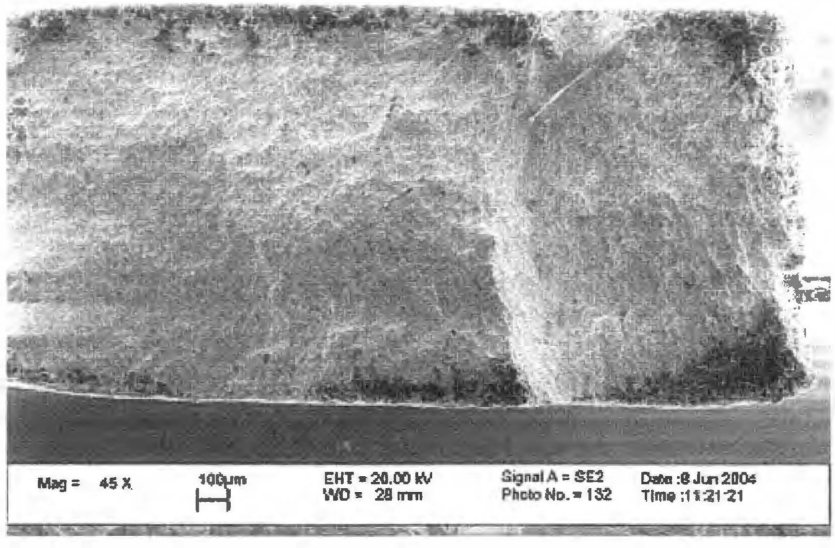

Figure C-21: Scanning Electron Microscopy of undoped Zircaloy-4 of specimen (C-Zr-3-1) on fracture surface exhibiting plastic deformation

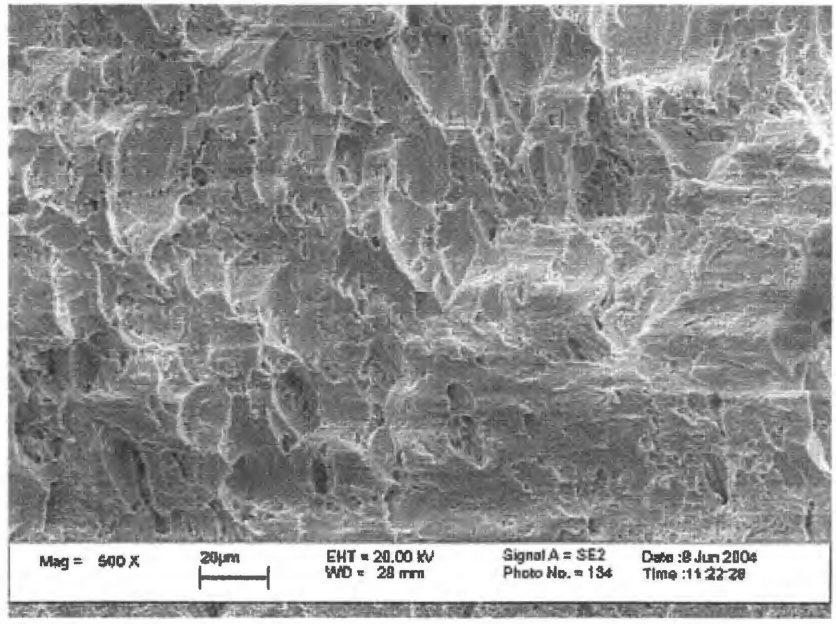

Figure C-22: Scanning Electron Microscopy of free Zircaloy-4 of specimen (C-Zr-3-3) on fracture surface spherical dimples and shear deformation

VITA

Chryso Kasongo Kahambwe was born in Lubumbashi, Democratic Republic of Congo, on September 21, 1967. He attended Saint-Boniface Primary School (Lubumbashi) and graduated in July 1980. In September 1981, he was admitted as a freshman at Athenee of Katuba High School; then in September 1983, he transferred to Maadini High School and majored in Science. In September 1984, he transferred to Kiwele (Lubumbashi) High School where he received the high school diploma in Biology and Chemistry in 1987. The following September, he was accepted at Polytechnic of University of Lubumbashi, majored in Chemical Engineering. He took one year off from college in 1988 and returned to college in 1989. In September 1990, he moved from Lubumbashi to Botswana via Zambia where he worked for one year as a machine operator at Spie Batignolles (French Company). In September 1993, he traveled to the United States and admitted as freshman at Nashville Technical Institution, Tennessee in 1994. In January 1995, he transferred to Tennessee States University and majored in Chemistry. In January1996, he transferred to University of Tennessee Knoxville, and received the Bachelor of Science degree in Chemical Engineering in December 1999. He worked for eight months as a field engineer at United Consulting Firm in Atlanta, Georgia. In January 2001, he returned to University of Tennessee Knoxville to continue graduate school, where he received the Masters of Science degree in Nuclear Engineering in December 2004, and interested to look for a nuclear engineering position or related field around the country.